Synaptopodin-associated ribosomal hubs regulate lesion-induced homeostatic plasticity at hippocampal mossy fiber synapses

Pia Kruse[1], Andreas Vlachos[1,2,3,§], Maximilian Lenz[1,§]

[1]Department of Neuroanatomy, Institute of Anatomy and Cell Biology, Faculty of Medicine, University of Freiburg, Freiburg, Germany.

[2]Center for Basics in Neuromodulation (NeuroModulBasics), Faculty of Medicine, University of Freiburg, Freiburg, Germany.

[3]Center Brain Links Brain Tools, University of Freiburg, Freiburg, Germany.

[§]Correspondence to andreas.vlachos@anat.uni-freiburg.de and maximilian.lenz@anat.uni-freiburg.de, Department of Neuroanatomy, Institute of Anatomy and Cell Biology, Faculty of Medicine, University of Freiburg, 79104 Freiburg, Germany

Keywords: homeostatic plasticity, denervation, synaptopodin, local protein synthesis

ABSTRACT

Neurological diseases can lead to the denervation of brain regions caused by demyelination, traumatic injury or cell death. Nevertheless, the molecular and structural mechanisms underlying the lesion-induced reorganization of denervated brain regions are a matter of ongoing investigation. In order to address this issue, we performed an entorhinal cortex lesion (ECL) in organotypic entorhinal-hippocampal tissue cultures and studied denervation-induced homeostatic plasticity of mossy fiber synapses, which connect dentate granule cells with CA3 pyramidal neurons and play important roles in spatial learning. Partial denervation caused a homeostatic strengthening of excitatory neurotransmission in dentate granule cells (GC), in CA3 pyramidal neurons, and their direct synaptic connections as revealed by paired recordings (GC-to-CA3). These functional changes were accompanied by ultrastructural reorganization of mossy fiber synapses, which regularly contain the plasticity-related protein synaptopodin and the spine apparatus organelle. We demonstrate that the spine apparatus organelle and its associated protein synaptopodin assemble ribosomes in close proximity to synaptic sites and moreover we unravel synaptopodin-related transcriptome, which can be linked to the expression of homeostatic synaptic plasticity. Notably, synaptopodin-deficient tissue preparations that lack the spine apparatus organelle, failed to express homeostatic adjustments of both excitatory neurotransmission and the region-specific transcriptome. Hence, synaptopodin and the spine apparatus organelle form local protein synthesis hubs that are essential for mediating lesion-induced homeostatic synaptic plasticity.

INTRODUCTION

Denervation is a common feature of various neurological diseases, which are accompanied by neuronal cell death, demyelination or traumatic injury of the central nervous system (Mesulam et al., 2019). As a result of the loss-of-input in otherwise healthy brain regions, complex reorganizational processes of neural circuits have been described. Among them, homeostatic synaptic plasticity has been established as an adaptive process of synaptic features that aims at compensating for perturbations of network activity (Turrigiano, 2012; Turrigiano, 2017; Vitureira et al., 2012). Specifically, excitatory synaptic strengthening upon denervation or activity deprivation has been reported as a compensatory synaptic adjustment (Turrigiano et al., 1998). Although homeostatic synaptic plasticity has been recognized as a local mechanism that can occur at distinct dendritic regions, the mechanisms that mediate dendritic autonomy in maintaining homeostasis remain unknown.

The hippocampal network is a crucial structure in memory acquisition. Here, the excitatory connection between dentate granule cells and CA3 pyramidal cells, i.e., the hippocampal mossy fiber synapse, has been demonstrated to play a crucial role in memory formation, maintenance and retrieval (Weng et al., 2018). Although numerous studies have addressed the unique plasticity features of this synapse (e.g. the onset of synaptic homeostasis and detonating transmission; (Lee et al., 2013)) and its impact on memory and behavior, no studies have addressed whether lesion-induced homeostatic synaptic plasticity occurs at this synapse when the main cortical excitatory input is affected, as seen for example in Alzheimer's disease (AD). In this context, organotypic tissue cultures of the entorhino-hippocampal complex provide the opportunity to study synaptic transmission at hippocampal mossy fiber synapses in a steady-state condition (Maus et al., 2020). Due to the laminated cortico-hippocampal input, the *in vitro* entorhinal-cortex lesion has been established as a model for the partial denervation of hippocampal neural circuits (Lenz et al., 2019; Prang et al., 2003; Vlachos et al., 2012a; Vlachos et al., 2012b).

In this study we used an entorhinal cortex lesion (ECL) of organotypic entorhino-hippocampal tissue cultures to study homeostatic adaptations in the dentate gyrus and CA3 network upon partial denervation. We provide evidence that partial denervation leads to excitatory synaptic strengthening in both dentate granule cells and CA3 pyramidal neurons. Using paired whole-cell patch-clamp recordings, we demonstrate changes in the synaptic transmission at hippocampal mossy fiber synapses that are accompanied by an ultrastructural reorganization of the spine apparatus organelle, which has previously been firmly linked to synaptic plasticity (Deller et al., 2003; Jedlicka and Deller, 2017; Jedlicka et al., 2009; Korkotian et al., 2014; Lenz et al., 2021a; Lenz et al., 2021b; Maggio and Vlachos, 2018; Vlachos et al., 2013; Vlachos et al., 2009). We demonstrate that synaptopodin and the spine apparatus organelle form ribosomal hubs that are linked to homeostatic plasticity-related local protein synthesis (Sutton et al., 2006). Consequently, synaptopodin-deficient tissue cultures, which lack the spine apparatus organelle, showed alterations in their ability to express homeostatic plasticity. Moreover, we demonstrate that synaptopodin-deficient tissue cultures have deficits in the denervation-induced adaptation of region-specific, i.e., dentate gyrus and CA3 transcriptomes. We therefore conclude, that

the spine apparatus organelle forms plastic local protein synthesis hubs that promote and mediate homeostatic synaptic adjustments upon partial denervation.

MATERIALS AND METHODS

Ethics statement

Mice were maintained in a 12 h light/dark cycle with food and water available ad libitum. Every effort was made to minimize distress and pain of animals. All experimental procedures were performed according to German animal welfare legislation and approved by the appropriate animal welfare committee and the animal welfare officer of Albert-Ludwigs-University Freiburg, Faculty of Medicine (X-17/07K, X-17/09K, X-21/01B).

Preparation of tissue cultures

Entorhino-hippocampal tissue cultures were prepared at postnatal day 3-5 from C57BL/6J (wildtype, Synpo$^{+/+}$) and B6.129-Synpo^{tm1Mndl}/Dllr [Synpo$^{-/-}$, (Deller et al., 2003; Lenz et al., 2021a; Lenz et al., 2021b)] mice of either sex as previously described (Del Turco and Deller, 2007). Cultivation medium contained 50% (v/v) MEM, 25% (v/v) basal medium eagle, 25% (v/v) heat-inactivated normal horse serum, 25 mM HEPES buffer solution, 0.15% (w/v) bicarbonate, 0.65% (w/v) glucose, 0.1 mg/ml streptomycin, 100 U/ml penicillin, and 2 mM glutamax. The pH was adjusted to 7.3. All tissue cultures were allowed to mature for at least 18 days in a humidified atmosphere with 5% CO_2 at 35°C. Cultivation medium was replaced 3 times per week.

Entorhinal cortex lesion (ECL)

The entorhinal cortex of mature slice cultures (≥18 days in vitro) was transected with a sterile scalpel from the rhinal to the hippocampal fissure to achieve a complete lesion of the perforant path. Except for the lesion-induced partial denervation of the hippocampus, cytoarchitecture of both the hippocampus and the entorhinal cortex remained unchanged.

Whole-cell patch-clamp recordings

Whole-cell patch-clamp recordings were carried out at 35°C (3-6 neurons per culture). The bath solution contained (in mM) 126 NaCl, 2.5 KCl, 26 $NaHCO_3$, 1.25 NaH_2PO_4, 2 $CaCl_2$, 2 $MgCl_2$, and 10 glucose (aCSF) and was oxygenated continuously (5% CO_2 / 95% O_2). Patch pipettes contained (in mM) 126 K-gluconate, 10 HEPES, 4 KCl, 4 ATP-Mg, 0.3 GTP-Na_2, 10 PO-Creatine, 0.3% (w/v) biocytin (pH 7.25 with KOH, 290 mOsm with sucrose), having a tip resistance of 4-6 MΩ. Pyramidal neurons were visually identified using a LN-Scope (Luigs & Neumann) equipped with an infrared dot-contrast and a 40x water-immersion objective (NA 0.8; Olympus). Spontaneous excitatory postsynaptic currents (sEPSCs) of both dentate granule cells and CA3 pyramidal neurons were recorded in voltage-clamp mode at a holding potential of −70 mV. Series resistance was monitored before and after each recording and recordings were discarded if the series resistance reached ≥ 30 MΩ. For recording of intrinsic cellular properties in current-clamp mode, pipette capacitance of 2.0 pF was corrected and series resistance was compensated using the automated bridge balance tool of the MultiClamp commander. I-

111 V-curves were generated by injecting 1 s square pulse currents starting at −100 pA and increasing in 10
112 pA steps until +500 pA current injection was reached (sweep duration: 2 s).
113
114 **Paired whole-cell patch-clamp recordings of hippocampal mossy fiber synapses**
115 Action potentials were generated in the presynaptic dentate granule cell by 5 ms square current pulses
116 (1 nA). For connectivity analysis, 5 action potentials were applied at 20 Hz respectively (inter-sweep-
117 interval: 10 sec; at least 30 repetitions), while recording unitary excitatory postsynaptic currents
118 (uEPSCs) from CA3 pyramidal cells. Neurons were considered to be connected if > 5 % of action
119 potentials evoked time-locked inward uEPSCs. Recordings were performed in the presence of (-)-
120 bicuculline-methiodide (10 µM, #ab120108 Abcam) to prevent inhibitory synapse recruitment.
121 Moreover, glutamine was added to the recording medium to avoid synapse depletion.
122
123 **Post hoc staining and imaging**
124 Tissue cultures were fixed overnight in a solution of 4% (w/v) paraformaldehyde (PFA; in PBS (0.1M,
125 pH 7.4) with 4% (w/v) sucrose). After fixation, cultures were washed in PBS (0.1 M, pH 7.4) and
126 consecutively incubated for 1 h with 10% (v/v) normal goat serum (NGS) in 0.5% (v/v) Triton X-100
127 containing PBS to reduce nonspecific staining. For post-hoc visualization of patched granule cells and
128 CA3 pyramidal cells, Streptavidin Alexa Fluor 488 (Streptavidin A488, 1:1000; #S32354 Invitrogen)
129 was added to the incubation solution. DAPI nuclear stain (1:5000 in PBS for 10 minutes; #62248
130 Thermo Scientific) was used to visualize cytoarchitecture. Cultures were washed, transferred onto glass
131 slides and mounted for visualization with DAKO anti-fading mounting medium (#S302380-2, Agilent).
132
133 **Transmission electron microscopy**
134 Wildtype (Synpo$^{+/+}$) and Synpo$^{-/-}$ tissue cultures were fixed in 4 % paraformaldehyde (w/v) and 2 %
135 glutaraldehyde (w/v) in 0.1 M phosphate buffer (PB) overnight and washed for 1 hour in 0.1 M PB.
136 After fixation, tissue cultures were sliced with a vibratome and the slices were incubated with 1 %
137 osmium tetroxide for 20 min in 5 % (w/v) sucrose containing 0.1 M PB. The slices were washed 5 times
138 for 10 min in 0.1 M PB and washed in graded ethanol [10 min in 10 % (v/v) and 10 min in 20 % (v/v)].
139 The slices were then incubated with uranyl acetate [1 % (w/v) in 70 % (v/v) ethanol)] overnight
140 and were subsequently dehydrated in graded ethanol 80 % (v/v), 90 % (v/v) and 98 % (v/v) for 10
141 min. Finally, slices were incubated with 100 % (v/v) ethanol twice for 15 min followed by two
142 15 min washes with propylene oxide. The slices were then transferred for 30 min in a 1:1
143 mixture of propylene oxide with durcupan and then for 1 hour in durcupan. The durcupan was
144 exchanged with fresh durcupan and the slices were transferred to 4 °C overnight. The slices were then
145 embedded between liquid release-coated slides and coverslips. Cultures were re-embedded in blocks
146 and ultrathin sections were collected on copper grids. Electron microscopy was performed at a LEO
147 906E microscope (Zeiss) at 4646x magnification.

148 **Regional mRNA library preparations and transcriptome analysis**

149 RNA Library preparations for transcriptome analysis were performed using the NEBNext® Single
150 Cell/Low Input RNA Library Prep Kit for Illumina® (New England Biolabs, #E6420) according to the
151 manufacturer's instructions. Briefly, isolation of the dentate gyrus and CA3 area from individual tissue
152 cultures was performed using a scalpel. One isolated dentate gyrus or CA3 area respectively was
153 transferred to 7.5 µl lysis buffer (supplemented with murine RNase inhibitor) and homogenized using a
154 pestill. Samples were centrifuged for 30 seconds at 10,000g and 5 µl of supernatant were collected from
155 individual samples and further processed. After cDNA synthesis, cDNA amplification was performed
156 according to the manufacturer's protocol with 12 PCR cycles. cDNA yield was consecutively analyzed
157 by a High Sensitivity DNA assay on a Bioanalyzer instrument (Agilent). cDNA amount was adjusted
158 to 10 ng for further downstream applications. After fragmentation and adaptor ligation, dual index
159 primers (New England Biolabs, #E7600S) were ligated in a library amplification step using 10 PCR
160 cycles. Libraries were finally cleaned up with 0.8X SPRI Beads following a standard bead purification
161 protocol. Library purity and size distribution was assessed with a High Sensitivity DNA assay on a
162 Bioanalyzer instrument (Agilent). We quantified the libraries using the NEBNext Library Quant Kit for
163 Illumina (New England Biolabs, #E7630) based on the mean insert size provided by the Bioanalyzer. A
164 10 nM sequencing pool (120 µl in Tris-HCl, pH 8.5) was generated for sequencing on the NovaSeq6000
165 Sequencing platform (Illumina; service provided by CeGaT GmbH, Tübingen, Germany). We
166 performed a paired-end sequencing with 101 bp read length. Data analysis was performed at the Galaxy
167 platform (usegalaxy.eu). All files contained more than 10 M high-quality reads (after mapping to the
168 reference genome; mm10) having at least a phred quality of 30 (>90% of total reads).

169

170 **Synaptopodin co-Immunoprecipitation (SP-coIP) and RT-qPCR analysis**

171 Six tissue cultures per biological replicate were washed in coIP-solution and dounce homogenized on
172 ice in a solution containing (150 µl per sample, coIP-solution, in mM): 10 HEPES, 120 NaCl, 0.05%
173 (v/v) NP-40, cOmplete protease inhibitor (Roche, according to manufacturers' instructions), murine
174 RNase inhibitor (1:1000, New England Biolabs, #M0314) and cycloheximide (0.5 mg/ml, Sigma
175 Aldrich, #C-4859). Input was precleared twice with protein A beads (10 µl per 100 µl
176 sample/supernatant) to reduce unspecific binding. Protein A beads (10 µl, New England Biolabs,
177 #S1425) were washed twice in coIP-solution and consecutively incubated for 1 hour at 4°C with an anti-
178 Synaptopodin antibody (rabbit anti-Synaptopodin, Synaptic Systems, #163002). Beads were carefully
179 washed twice to remove unbound antibodies and incubated for 1 hour with the precleared supernatant
180 ('input') at 4°C with head-over-tail rotation. 10 µl of the precleared supernatant were kept as input
181 control. After incubation, beads were washed twice with coIP-solution and finally dissolved in RNA
182 protection buffer (New England Biolabs). RNA was released from the beads through Protein K lysis
183 (Monarch® Total RNA Miniprep Kit; #T2010S New England Biolabs). After lysis, beads were removed
184 from the solution in a magnetic rack and the RNA containing supernatant was transferred to fresh tubes.

185 RNA isolation on coIP- and input-samples was then performed according to the manufacturer's
186 instructions. RNA content was determined using the Agilent RNA 6000 Pico Kit (#5067-1513 Agilent)
187 with a 2100 Bioanalyzer (#G2939BA Agilent). Purified RNA was consecutively reverse transcribed
188 (RevertAid RT Kit; #K1691 Thermo Scientific). cDNA was diluted in water to a final concentration of
189 0.2 ng/µl. RT-qPCR was performed using a C1000 Touch Thermal Cycler (BIO-RAD) and the CFX
190 384 Real-Time PCR system (BIO-RAD). 0.9 ng target cDNA diluted in TaqMan Gene Expression
191 Master Mix (Applied Biosystems #4369016) were amplified using standard TaqMan Gene Expression
192 Assays (Applied Biosystems; Assay-IDs: Gapdh: Mm99999915_g1; Gria1: Mm00433753_m1). RNA
193 Library preparations for Synpo-related transcriptome analysis were performed using the NEBNext®
194 Single Cell/Low Input RNA Library Prep Kit for Illumina® (New England Biolabs, #E6420) according
195 to the manufacturer's instructions. We quantified the libraries using the NEBNext Library Quant Kit for
196 Illumina (New England Biolabs, #E7630) based on the mean insert size provided by the Bioanalyzer. A
197 10 nM sequencing pool (120 µl in Tris-HCl, pH 8.5) was generated for sequencing on the NovaSeq6000
198 Sequencing platform (Illumina; service provided by CeGaT GmbH, Tübingen, Germany). We
199 performed a paired-end sequencing with 151 bp read length. Data analysis was performed at the Galaxy
200 platform (usegalaxy.eu). All files contained more than 10 M high-quality reads (after mapping to the
201 reference genome; mm10) having at least a phred quality of 30 (>90% of total reads).
202
203 **Quantification and statistics**
204 Electrophysiological data were analyzed using pClamp 10.7 (Axon Instruments) and MiniAnalysis
205 (Synaptosoft) software. The fraction of action potentials followed by time-locked excitatory
206 postsynaptic current responses was considered as synaptic response rate. uEPSC amplitude was assessed
207 in uEPSCs from successfully transmitted action potentials as well as the mean amplitude of all
208 successfully evoked postsynaptic responses. In order to ensure selective analysis of time-locked
209 responses, events were included if > 5% of presynaptic pulses were successfully transmitted for each
210 pulse respectively. For individual pulses that caused ≤ 5% successfully transmitted events, response rate
211 was set to '0'. EPSC properties were analyzed using the automated template search tool for event
212 detection (Lenz et al., 2021b). In order to perform a hierarchical analysis of sEPSCs, all events of a
213 recorded cell were sorted based on their peak amplitude. Events above the 50th percentile therefore
214 correspond to all events above the cells median amplitude of events. Input resistance was calculated for
215 the injection of –100 pA current at a time frame of 200 ms with a maximum distance to the initial
216 hyperpolarization. Resting membrane potential was calculated as the mean baseline value. AP detection
217 was performed using the input-output curve threshold search event detection tool, and the AP frequency
218 was assessed by the number of APs detected during the respective current injection time. Ultrastructural
219 features were analyzed by an investigator blind to experimental conditions in randomly selected mossy
220 fiber terminals from electron micrographs of the stratum lucidum in non-lesioned and lesioned wildtype
221 tissue cultures.

RT-qPCR data were analyzed as previously described (Lenz et al., 2020) with the Bio-Rad CFX Maestro 1.0 software package using the ΔΔCq method with Gapdh as reference gene. Values were normalized to the mean value of the respective control group.

Electron microscopy images were saved as TIF-files and analyzed using the ImageSP Viewer software (http://e.informer.com/sys-prog.com).

RNA sequencing data were uploaded to the Galaxy web platform (public server: usegalaxy.eu; (Afgan et al., 2018; Galaxy, 2022; Goecks et al., 2010)) and transcriptome analysis was performed using the Galaxy platform in accordance with the reference-based RNA-seq data analysis tutorial (Batut et al., 2021). Adapter sequencing, low quality, and short reads were removed via the CUTADAPT tool (Galaxy version 3.5+galaxy0). Reads were mapped using RNA STAR (Galaxy version 2.7.8a+galaxy0) with the mm10 full reference genome (Mus musculus). The evidence-based annotation of the mouse genome (GRCm38), version M25 (Ensembl 100), served as gene model (GENCODE). For an initial assessment of gene expression, unstranded FEATURECOUNT (Galaxy version 2.0.1+galaxy2) analysis was performed from RNA STAR output. Only samples that contained >60% uniquely mapping reads (feature: "exon") were considered for further analysis. Statistical evaluation was performed using DESeq2 (Galaxy version 2.11.40.7+ galaxy1) with "pathway integrity" as the primary factor that might affect gene expression. Genes with a low number of mean reads (< 300 BaseMean) were excluded from further analysis. Genes were considered as differentially expressed if the adjusted p-value was < 0.05. Data visualization was performed according to a modified version of a previously published workflow (Reimand et al., 2019). A ranked list for the gene set enrichment analysis was generated based on Wald-Stats from the DeSeq2 output. For the consecutive gene set enrichment analysis, we have used the GSEA software package ((Mootha et al., 2003; Subramanian et al., 2005); BROAD institute; version GSEA_4.2.1) with integrated MSigDB gene sets. Enrichment maps were built using cytoscape ((Shannon et al., 2003); version 3.9.0) with the EnrichmentMap application. Heatmaps were generated based on z-scores of the normalized count table.

Data were statistically analyzed using GraphPad Prism 7 (GraphPad software, USA). All values represent mean ± standard error of the mean. For statistical comparison of two experimental groups, a Mann-Whitney test was employed. Short-term plasticity experiments were statistically assessed by the repeated measure (RM) two-way ANOVA test with Sidak's (two groups) or Tukey's (three groups) multiple comparisons test. uEPSC amplitude values from individual cells were stacked in subcolumns and the pulse number was defining tabular rows (COLUMN factor: pathway, genetic background or recombination; ROW factor: pulse number). P-values < 0.05 were considered statistically significant (*p < 0.05, **p < 0.01, ***p < 0.001); results that did not yield significant differences are designated 'ns'. Statistical differences in XY-plots were indicated in the legend of the figure panels (*) when detected through multiple comparisons, irrespective of their localization and the level of significance. In the text and figures, values represent the mean ± standard error of the mean (s.e.m.).

Digital illustrations

Confocal image stacks were stored as TIF files. Figures were prepared using the ImageJ software package (https://imagej.nih.gov/ij/) and Photoshop graphics software (Adobe, San Jose, CA, USA). Image brightness and contrast were adjusted.

263 **RESULTS**

264 **Entorhinal cortex lesion leads to homeostatic synaptic plasticity in both dentate granule cells and**
265 **CA3 pyramidal neurons**

266 Entorhinal cortex lesion was performed in mature tissue cultures to achieve a complete dissection of the
267 perforant path leading to a partial denervation of both dentate granule cells and CA3 pyramidal neurons
268 (Figure 1A). Spontaneous excitatory postsynaptic currents (sEPSCs) were recorded from dentate
269 granule cells and CA3 pyramidal neurons in non-lesioned control and lesioned tissue cultures (3 days
270 post entorhinal cortex lesion, 3dp ECL) to assess denervation-induced effects on excitatory
271 neurotransmission (Figure 1B). As previously described [e.g., (Lenz et al., 2019; Vlachos et al., 2012b)],
272 partial denervation caused a strengthening of excitatory synapses in dentate granule cells, i.e., a
273 significant increase in both the mean sEPSC amplitude and half width as well as the mean sEPSC area
274 (Figure 1C). A consecutive percentile analysis revealed that the lesion-induced increase in sEPSC
275 amplitudes is evident when comparing the 50% biggest events in both groups while no effect was
276 observed when comparing smaller events (Figure 1D). Notably, a significant upregulation in the mean
277 sEPSC frequency was observed after lesion (Figure 1E) that resulted from an increased abundance of
278 high amplitude sEPSC events as revealed by the amplitude/frequency-plot (Figure 1F).
279 Next, we examined excitatory neurotransmission in CA3 pyramidal neurons in non-lesioned and
280 lesioned cultures (3dp ECL; Figure 1G-J). Again, a significant increase in both the mean sEPSC
281 amplitude and area was observed in CA3 cells from lesioned cultures indicating a denervation-induced
282 excitatory synaptic strengthening (Figure 1G). Notably, the mean sEPSC half width remained
283 unchanged. In the sEPSC amplitude percentile analysis, excitatory synaptic strengthening seems to be
284 restricted to the high amplitude events (Figure 1H). Moreover, the mean sEPSC frequency remained
285 unchanged upon ECL (Figure 1I), which resulted from an increase in the abundance of high amplitude
286 events (in the sEPSC amplitude range from 80-110 pA, RM two-way ANOVA followed by Sidak's
287 multiple comparisons test) at the expense of small amplitude events (Figure 1J). We therefore conclude
288 that ECL leads to a homeostatic increase in excitatory neurotransmission in both dentate granule cells
289 and CA3 pyramidal neurons.
290

291 **Partial denervation does not cause changes in intrinsic cellular properties**

292 Passive and active membrane properties were assessed in both dentate granule cells (Figure S1A-C) and
293 CA3 pyramidal neurons (Figure S1D-F) to test for homeostatic adaptations of intrinsic cellular
294 properties upon lesion. In dentate granule cells no changes in passive membrane properties (Figure
295 S1A), i.e., the resting membrane potential (RMP) and the input resistance as well as the input-output
296 curve dynamics were observed (Figure S1B). Additionally, the action potential frequency of dentate
297 granule cells was similar in lesioned and non-lesioned cultures (Figure S1C). Noteworthy, RMP
298 assessment confirmed the mature state of the recorded dentate granule cells [c.f. (Strehl et al., 2018)].

299 Concerning CA3 pyramidal neurons, neither the passive membrane properties (Figure S1D) – including
300 input-output curve dynamics (Figure S1E) – nor the active properties (Figure S1F) were changed. Based
301 on these results, we conclude that intrinsic cellular properties were stable following denervation in both
302 tested cell types of the hippocampal network.
303
304 **Entorhinal cortex lesion induces changes in synaptic transmission at hippocampal mossy fiber**
305 **synapses**
306 Hippocampal mossy fiber synapses have previously been linked to learning processes and memory
307 formation (Lipp et al., 1988; Vandael et al., 2020). Concerning their synaptic features, they have been
308 described as synapses that generate large postsynaptic currents upon activation (Henze et al., 2002a).
309 Given that our results demonstrate changes in both investigated regions, which additionally hint towards
310 a preferential lesion-related plasticity induction in readily strong synapses at CA3 pyramidal neurons,
311 we next assessed the features of synaptic transmission at hippocampal mossy fiber synapses.
312 Therefore, we performed paired whole-cell patch-clamp recordings of individual dentate granule cells
313 and CA3 pyramidal neurons in organotypic tissue cultures (Figure 2A). To test for synaptic connections,
314 5 consecutive action potentials at 20 Hz frequency were elicited in dentate granule cells (Figure 2B).
315 Unitary excitatory postsynaptic currents (uEPSCs) were monitored in CA3 pyramidal neurons in non-
316 lesioned and lesioned tissue cultures. We found that a train of presynaptic action potentials in connected
317 neurons induced a robust facilitation of postsynaptic responses in both postsynaptic response rate and
318 uEPSC amplitude under baseline conditions (Figure 2B-D). Notably, the response rate to the first
319 presynaptic action potential, which is the number of presynaptic action potentials that generate a
320 postsynaptic response, was very low (~3%; Figure 2C). In lesioned cultures, however, a significant
321 increase in the synaptic reliability for the first two pulses was observed. For the last three pulses in one
322 train of stimulation, averaged synaptic response rate levels became similar (Figure 3C). Moreover, the
323 uEPSC amplitude was significantly increased in response to the individual pulses 3 days after ECL
324 (Figure 2D). This novel approach of GC-to-CA3 paired recordings in the steady-state environment of
325 organotypic tissue cultures provided evidence that synaptic transmission at hippocampal mossy fiber
326 synapses is a target for lesion-induced remodeling of hippocampal networks.
327
328 **Synaptopodin and the spine apparatus organelle represent dendritic ribosomal hubs that are**
329 **associated with excitatory synapse related mRNAs**
330 Hippocampal mossy fiber synapses show a complex organization of their pre- and postsynaptic sites.
331 Among these features, a regular occurrence of the spine apparatus organelle, which is a transmission-
332 and plasticity-regulating organelle, has been reported at the postsynaptic site (Chicurel and Harris,
333 1992). We hypothesized that the spine apparatus organelle and its associated protein synaptopodin
334 mediate their effects on mossy fiber plasticity by interfering with local protein synthesis. Using
335 transmission electron microscopy, a close interaction between ribosomes and the spine apparatus

336 organelle was readily revealed (Figure 3A). To test whether synaptopodin, which is a marker protein
337 and essential component of the spine apparatus organelle (Deller et al., 2003), interacts with local
338 translation machineries, i.e., dendritic ribosomes, we performed synaptopodin co-immunoprecipitation
339 (Synpo-coIP) experiments with subsequent RT-qPCR analysis. Using RNA assessment on a
340 Bioanalyzer, we found rRNA peaks in Synpo-coIP experiments whereas no rRNA was detected in bead-
341 only controls (Figure 3B). RT-qPCR analysis (reference gene: Gapdh) from input and Synpo-coIP
342 samples revealed that the Gria1 mRNA, which has been linked to synaptopodin-dependent synaptic
343 plasticity (Vlachos et al., 2009) and homeostatic synaptic plasticity (Aoto et al., 2008; Sutton et al.,
344 2006), is significantly enriched in Synpo-coIP samples (Figure 3C). We therefore conclude, that
345 synaptopodin and the spine apparatus organelle might serve as a ribosomal hub that significantly
346 contributes to plasticity-related local protein synthesis.
347 To further unravel the plasticity-mediating features of synaptopodin and the spine apparatus organelle,
348 we performed a transcriptome analysis of Synpo-coIP enriched mRNA (Figure 3D, Table S1). A
349 considerable amount of mRNAs were enriched after Synpo-coIP compared to input samples: 2355
350 mRNAs showed a higher abundance in Synpo-coIP samples compared to the respective input samples
351 (UP). Subsequently, a gene set enrichment analysis (GSEA) was performed to elucidate the functional
352 relevance of synaptopodin-associated mRNAs (Figure 3E, Table S2). We identified distinct clusters of
353 cellular compartment gene sets that have been enriched by Synpo-coIP. Among them, synapse and actin
354 cytoskeleton-related gene sets were identified that have been linked to synaptic plasticity. Of note, these
355 data suggest the synaptopodin-dependent assembly of localized organelle associated transcriptome hubs
356 that can be dedicated to local protein synthesis.
357
358 **The synaptopodin-associated transcriptome remains stable upon lesion**
359 We next tested whether the composition of the synaptopodin-associated transcriptome changes in
360 lesioned networks 3dp ECL. Therefore, a differential mRNA abundance analysis was performed in
361 Synpo-coIP and their respective input RNA samples from lesioned and non-lesioned wildtype cultures
362 (Figure S2). In mRNA libraries prepared from input RNA samples, we found a considerable amount of
363 differentially expressed genes upon ECL (Table S3). In contrast, a limited amount of mRNAs were
364 differentially enriched upon ECL in Synpo-coIP samples (Table S4). We therefore conclude that the
365 composition of the synaptopodin-associated transcriptome remain stable upon partial denervation.
366
367 **Ultrastructural reorganization of the ribosome associated spine apparatus organelle**
368 Previous studies have demonstrated that the ultrastructural organization of the spine apparatus organelle
369 might represent a target for plasticity (Lenz et al., 2021b; Vlachos et al., 2013). To study lesion-induced
370 effects on the ultrastructural organization of the ribosome associated spine apparatus organelle that
371 might interfere with local protein synthesis, we performed transmission electron microscopy of mossy
372 fiber synapses in non-lesioned and lesioned (3dp ECL) entorhino-hippocampal tissue cultures (Figure

373 3F; c.f., (Vlachos et al., 2013)). No differences in the structural organization of pre- and postsynaptic
374 sites could be detected between the groups (presynapse: mossy fiber perimeter: 11.61 ± 0.4 µm (control;
375 n = 120) vs. 10.88 ± 0.35 µm (3dp ECL; n = 90); postsynapse: number of PSDs: 4.91 ± 0.33 (control; n
376 = 120) vs. 4.6 ± 0.27 (3dp ECL; n = 90), length of PSDs: 201 nm ± 4.35 (control; n = 589) vs. 201.7 ±
377 5.42 nm (3dp ECL; n = 414); values indicate mean ± sem, Mann-Whitney test). Nevertheless, a
378 substantial reorganization of the spine apparatus organelle was evident in lesioned cultures 3 days after
379 injury compared to non-lesioned controls (Figure 3G, H). We found a significantly increased number
380 of dense plates in spine apparatus organelles from lesioned cultures (Figure 3G). At the same time the
381 length of individual dense plates was significantly reduced in lesioned cultures (Figure 3H). Therefore,
382 we conclude that the spine apparatus organelle, which is an mRNA hub for local protein synthesis,
383 represents a target for lesion-induced changes at hippocampal mossy fiber synapses.
384
385 **Synaptopodin-deficient tissue cultures show deficits in homeostatic synaptic plasticity upon**
386 **partial denervation**
387 Based on our ultrastructural analysis, we hypothesized that the reorganization of the spine apparatus
388 organelle might contribute to homeostatic synaptic plasticity at hippocampal mossy fiber synapses. To
389 gain further insights concerning the role of the spine apparatus organelle in this adaptive process, we
390 performed experiments in synaptopodin-deficient tissue preparations, which lack the spine apparatus
391 organelle (Figure 4; (Deller et al., 2003)).
392 Synaptopodin-deficient dentate granule cells showed a significant increase in both the mean sEPSC
393 amplitude and area as well as the mean sEPSC half width 3 days following ECL (Figure 4A). In contrast,
394 no changes in the mean sEPSC frequency, which have been observed in wildtype (Synpo$^{+/+}$) cultures,
395 were detected (Figure 4B). Moreover, passive membrane properties remained stable upon lesion in
396 synaptopodin-deficient tissue preparations (Figure 4C).
397 When assessing excitatory neurotransmission onto CA3 pyramidal neurons in lesioned and non-lesioned
398 cultures, no significant changes in the sEPSC event analysis (Figure 4D) or the mean sEPSC frequency
399 (Figure 4E) were observed. Again, passive membrane properties remained unchanged (Figure 4F).
400 Thus, we here provide evidence for deficits in the implementation of homeostatic synaptic adaptations
401 for both dentate granule cells and CA3 pyramidal neurons in synaptopodin-deficient tissue cultures.
402 We extended these findings with GC-to-CA3 paired whole-cell patch-clamp recordings in
403 synaptopodin-deficient preparations (Figure 4G). In contrast to wildtype cultures, no significant
404 differences in the synaptic reliability could be detected 3 days after ECL (Figure 4H). When analyzing
405 the uEPSC amplitude of successfully transmitted events, surprisingly, we found a significant reduction
406 in the pulse-related uEPSC amplitude in lesioned synaptopodin-deficient preparations (Figure 4I), while
407 excitatory neurotransmission seemed facilitated under baseline conditions as compared to wildtype
408 cultures (Figure S3). Hence, synaptopodin-deficient mossy fiber synapses responded in a synaptic
409 depression rather than homeostatic synaptic strengthening after the lesion. These findings demonstrate

410 the role of the postsynaptic spine apparatus organelle on plasticity of mossy fiber synapses. They are
411 consistent with recent work that suggested a role of synaptopodin and the spine apparatus in mediating
412 metaplasticity (Hulme et al., 2014; Lenz et al., 2021a).
413
414 **Entorhinal cortex lesion causes synaptopodin-dependent changes in the region-specific**
415 **hippocampal transcriptome**
416 To further unravel lesion-induced changes in hippocampal subfields that might depend on synaptopodin,
417 we performed transcriptome analysis of both the dentate gyrus and the CA3 region in non-lesion and
418 lesioned cultures from wildtype (Synpo$^{+/+}$) and synaptopodin-deficient (Synpo$^{-/-}$) animals (Figure 5).
419 The expression analysis revealed a considerable number of genes that are differentially expressed in
420 both hippocampal regions from wildtype animals (Figure 5A, B). In contrast, synaptopodin-deficient
421 tissue culture preparations showed deficits in the lesion-induced adjustment of gene expression in CA3
422 whereas in the dentate gyrus it remained evident (Figure 5A). Moreover, we demonstrate that wildtype
423 and synaptopodin-deficient tissue preparations show a genotype dependent gene expression adjustment
424 upon lesion in both regions although a common set of regulated genes has been identified (Figure 6B;
425 for detailed tabular results see supplementary tables S5-S8). We therefore conclude, that synaptopodin
426 might act as a sensor that triggers differential gene expression towards homeostatic adjustments in a
427 region-specific fashion.
428 The subsequently performed geneset enrichment analysis with an additional enrichment map
429 visualization (GSEA, Figure 5C) provided evidence that the ECL caused an inflammatory response in
430 the hippocampus of wildtype cultures that might result from the accumulation of microglia. Moreover,
431 partial denervation is accompanied by changes in metabolic gene sets (metabolic clusters), differences
432 in membrane organization and a potential impact on neurogenesis. Further assessment of the
433 differentially expressed genes suggested that these changes might be the result of a region-specific
434 microglia accumulation in the denervated areas.
435 In order to learn more about the lesion-induced differential expression of genes that have been linked to
436 synaptic plasticity ("synapse" GOCC: 0045202), the region-specific lists of differentially expressed
437 genes were filtered according to the content of the respective gene ontology (Figure 5D). We found
438 numerous synaptic genes in both regions that show a differential expression upon lesion, which
439 corresponds to the functional assessment of synaptic transmission where a strengthening of excitatory
440 neurotransmission was observed. Therefore, we conclude that the lesion-induced change in the region-
441 specific transcriptome might represent an essential component of the homeostatic synaptic response.
442

443 **DISCUSSION**

444 Denervation is a common phenomenon in numerous medical conditions affecting the central nervous
445 system, which can trigger homeostatic adaptations in neural networks (Barnes et al., 2017; Bissen et al.,
446 2021; Hengen et al., 2013; Lambo and Turrigiano, 2013; Platschek et al., 2016; Vlachos et al., 2012b).
447 In this study, we have unraveled a novel feature of the spine apparatus organelle that crucially
448 contributes to the localized expression of compensatory synaptic changes. In line with previous findings
449 that employed proximity proteomics of synaptopodin (Falahati et al., 2022), we identified a close
450 interaction between synaptopodin and ribosomes. Using subsequent synaptopodin co-
451 immunoprecipitation experiments, we here elucidated the synaptopodin-related transcriptome, which
452 might contribute to plasticity-related local protein synthesis. Together with findings that indicate
453 interactions between synaptopodin and ER-related proteins (Falahati et al., 2022), we suggest a role for
454 synaptopodin and the spine apparatus organelle as local plasticity hubs in neuronal dendrites.

455 To study lesion-induced changes in synaptic transmission, we used the *in vitro* model of ECL in
456 organotypic entorhino-hippocampal tissue cultures to study the effects of a partial loss of input on
457 hippocampal synaptic transmission. After *in vitro* maturation, tissue organization has reached a steady-
458 state that is characterized by structural and functional stability of excitatory synapses and that resembles
459 the ultrastructural synaptic architecture *in vivo* (Haber et al., 2006; Heller and Rusakov, 2017). In this
460 context, recent work has demonstrated that organotypic hippocampal tissue cultures have intact mossy
461 fiber pathways and synapses (Maus et al., 2020). Moreover, tissue cultures of the hippocampal
462 formation show an *in vivo* like cellular architecture and a preserved lamination in which the excitatory
463 cortical input – the perforant path – terminates at distal apical dendrites of dentate granule cells and
464 pyramidal neurons of the ammonic subregions (Frotscher and Heimrich, 1995; Frotscher et al., 1997;
465 Frotscher et al., 1995). Our results provide evidence for homeostatic excitatory synaptic plasticity in
466 both dentate granule cells and CA3 pyramidal neurons upon lesion, which is accompanied by changes
467 in the region-specific transcriptome and the abundance of synapse-related mRNAs. Moreover, we here
468 established a novel method to assess synaptic transmission at individual hippocampal mossy fiber
469 synapses – the monosynaptic excitatory contacts between dentate granule cells and CA3 pyramidal
470 neurons – in a steady-state environment by paired whole-cell patch-clamp recordings of connected
471 neurons. In this experimental approach, we identified synaptic transmission at hippocampal mossy fiber
472 synapses as a target for denervation induced synaptic plasticity. In addition, ultrastructural changes in
473 the spine apparatus organelle, which is well established in the regulation of synaptic plasticity (Lenz et
474 al., 2021b; Vlachos et al., 2013), can be observed after ECL. Since homeostatic adaptations on both
475 synaptic and transcriptomic levels were altered in synaptopodin-deficient animals which lack the spine
476 apparatus organelle, we conclude its crucial role in mediating as well as sensing and triggering
477 compensatory synaptic changes.

478 The dentate gyrus/CA3 neural network is an integral component of the memory-associated trisynaptic
479 hippocampal pathway. The hippocampal mossy fiber pathway forms large *en passant* synapses and

480 connects one individual granule cell to a limited number of CA3 pyramidal neurons (Acsady et al.,
481 1998). Both regions receive cortical input – the perforant path – from entorhinal layer II stellate cells
482 that can induce, promote and modulate information processing in hippocampal subregions. Moreover,
483 this pathway is a well-established target for various diseases; among them traumatic, inflammatory and
484 neurodegenerative conditions like Alzheimer's disease (AD; (Robinson et al., 2014; Thal et al., 2000)).
485 Here, we demonstrate that both dentate granule cells and CA3 pyramidal neurons express synaptic
486 plasticity upon partial denervation, which suggests that information processing at the connection
487 between these cells might be affected.
488 The expression of synaptic plasticity in the hippocampal neural circuit is involved in crucial aspects of
489 normal brain function, such as learning and memory acquisition. The hippocampal mossy fiber synapse,
490 which is the monosynaptic excitatory connection between dentate granule cells and CA3 pyramidal
491 neurons, has previously been described as an integral component of this network that relates to distinct
492 forms of memory acquisition and retrieval (Hunsaker et al., 2008; Marr, 1971). Specifically, activity-
493 dependent structural and functional changes in synaptic architecture and transmission have been found
494 to encode distinct input patterns for a prolonged period of time (Lee et al., 2013; Vandael et al., 2020).
495 Notably, alterations in hippocampal mossy fiber transmission have been reported in animal models of
496 Alzheimer's disease (AD) and aging related cognitive decline (Viana da Silva et al., 2019; Villanueva-
497 Castillo et al., 2017) where a particular loss in cortical input pathways onto hippocampal neurons can
498 be found. Nevertheless, it remains unclear if the lesion-induced synaptic response deteriorates cognitive
499 performance. Given that (1) homeostatic synaptic plasticity is altered in synaptopodin-deficient tissue
500 preparations and (2) alterations in synaptopodin expression have been linked to cognitive decline
501 (Wingo et al., 2019), we suggest that synaptopodin-mediated synaptic stability as well as compensatory
502 plasticity aim at maintaining proper network function.
503 Recently, characteristic features of transmission and stabilizing factors at hippocampal mossy fiber
504 synapses have been reported (De Bruyckere et al., 2018; Vandael et al., 2021b; Vyleta et al., 2016;
505 Vyleta and Jonas, 2014). Upon presynaptic activity, a detonating behavior can be observed in which a
506 limited number of – but not single – action potentials can elicit a suprathreshold postsynaptic
507 depolarisation (Henze et al., 2002b). Although this phenomenon has been extensively described in
508 mossy fiber bouton-CA3 pyramidal cell paired recordings (Vandael et al., 2021a), we were not able to
509 reveal detonating characteristics in granule cell-CA3 pyramidal cell pairs. Here, we assume that both
510 differences in the experimental model and methodology can account for these differences, which
511 warrant further clarification in future studies. Nevertheless, a filtering of single action potentials with a
512 subsequent robust facilitation of synaptic transmission at this synapse was evident, which is in line with
513 previous reports demonstrating an initially low presynaptic release probability with consecutive
514 facilitation (Gundlfinger et al., 2007; Zalutsky and Nicoll, 1990). Our results demonstrate that the partial
515 loss of input following lesion can influence both synaptic reliability and potency, which has been
516 observed for other plasticity-inducing stimuli at this synapse (Zalutsky and Nicoll, 1990). We suggest

517 that lesion-induced modulation of dual filtering/facilitation properties at connected pairs of dentate
518 granule cells and CA3 pyramidal neurons might interact with both pattern separation and completion
519 along the dentate gyrus/CA3 axis in a way that the increase in synaptic reliability and potency may shift
520 the balance towards pattern completion rather than separation (Leutgeb et al., 2007; O'Reilly and
521 McClelland, 1994; Prince et al., 2016). Moreover, the presence of synaptopodin will presumably
522 interfere with this network process under baseline and plasticity-inducing conditions which might
523 account for the previously reported cognitive deficits in synaptopodin-deficient mice (Deller et al.,
524 2003) and the synaptopodin-related cognitive decline during human aging (Wingo et al., 2019).
525 Furthermore, it is an established view that mossy fiber synaptic plasticity is predominantly mediated by
526 presynaptic processes (Monday et al., 2022; Orlando et al., 2021; Vandael et al., 2020). Nevertheless,
527 recent work has suggested that the postsynaptic site shapes the transmission and plasticity through
528 transsynaptic mechanisms (Vandael et al., 2021b). In this study, we provide evidence that the
529 postsynaptically located spine apparatus organelle mediates denervation-induced synaptic plasticity at
530 this synapse. Since its discovery, the function of the spine apparatus organelle and the mechanisms
531 through which it orchestrates synaptic plasticity remained enigmatic. We here demonstrate that
532 synaptopodin and the spine apparatus organelle represent dendritic ribosomal hubs that contribute to
533 plasticity-driven local protein synthesis. The lesion-induced ultrastructural remodeling of the spine
534 apparatus organelle might therefore represent a novel regulatory mechanism for localized changes in
535 synaptic transmission (Dubes et al., 2022; Vlachos et al., 2009).
536 Notably, we found opposing plasticity phenomena at hippocampal mossy fiber synapses on the level of
537 individual neuron pairs in wildtype and synaptopodin-deficient tissue preparations where synaptopodin
538 deficiency did not only cause defects in plasticity expression but hampered the ability of neurons to
539 maintain synaptic stability upon lesion. While the loss of input in wildtype cultures led to a significant
540 homeostatic strengthening of DG-CA3 excitatory synaptic transmission, synaptopodin deficiency was
541 associated with a lesion-related loss of synaptic potency. We therefore conclude that the function of the
542 spine apparatus organelle and its related protein synaptopodin might not be restricted to the mediation
543 of receptor accumulation at postsynaptic sites but rather comprises the implementation of plasticity
544 directionality (Vlachos, 2012). However, the link between synaptopodin and recently described
545 mechanisms that switch plasticity directionality from homeostatic to associative rules remain to be
546 determined (Wu et al., 2022). On the other hand, the lack of synaptopodin might decrease synaptic
547 resilience due to the lack of stabilizing features (Yap et al., 2020), which is required to maintain synaptic
548 transmission upon lesion. Regardless of these considerations, once more we report that synaptopodin
549 and the spine apparatus organelle act as crucial regulators of synaptic plasticity.
550 Moreover, synaptic transcriptional changes as seen in wildtype cultures were absent in synaptopodin-
551 deficient cultures. Since the differential expression of lesion-related inflammatory genes that might
552 promote plasticity induction was not observed in synaptopodin-deficient cultures, a link between
553 synaptopodin and proinflammatory plasticity promotion might exist (Eichler et al., 2022; Strehl et al.,

554 2014). Due to these observations, we suggest a dual role for synaptopodin as activity sensor and
555 plasticity effector, which assembles synapse-related mRNAs at dendritic plasticity hubs.

ACKNOWLEDGEMENTS

The Galaxy server that was used for some calculations in this study is partially funded by Collaborative Research Centre 992 Medical Epigenetics (DFG grant SFB 992/1 2012) and German Federal Ministry of Education and Research (BMBF grants 031 A538A/A538C RBC, 031L0101B/031L0101C de.NBI-epi, and 031L0106 de.STAIR (de.NBI)). We thank Bernd Heimrich for helpful and stimulating discussions on ultrastructural mossy fiber architecture. Moreover, we thank Sigrun Nestel for excellent technical assistance in electron microscopy. This work was supported by Else Kröner-Fresenius-Stiftung (EKFS_#2019_A94 to ML) and Deutsche Forschungsgemeinschaft (DFG; Project-ID 259373024 B14–CRC/TRR 167 to AV).

565 **REFERENCES**

566 Acsady, L., Kamondi, A., Sik, A., Freund, T., and Buzsaki, G. (1998). GABAergic cells are the major
567 postsynaptic targets of mossy fibers in the rat hippocampus. J Neurosci *18*, 3386-3403.

568 Afgan, E., Baker, D., Batut, B., van den Beek, M., Bouvier, D., Cech, M., Chilton, J., Clements, D.,
569 Coraor, N., Gruning, B.A., *et al.* (2018). The Galaxy platform for accessible, reproducible and
570 collaborative biomedical analyses: 2018 update. Nucleic Acids Res *46*, W537-W544.

571 Aoto, J., Nam, C.I., Poon, M.M., Ting, P., and Chen, L. (2008). Synaptic signaling by all-trans retinoic
572 acid in homeostatic synaptic plasticity. Neuron *60*, 308-320.

573 Barnes, S.J., Franzoni, E., Jacobsen, R.I., Erdelyi, F., Szabo, G., Clopath, C., Keller, G.B., and Keck,
574 T. (2017). Deprivation-Induced Homeostatic Spine Scaling In Vivo Is Localized to Dendritic Branches
575 that Have Undergone Recent Spine Loss. Neuron *96*, 871-882 e875.

576 Batut, B., van den Beek, M., Doyle, M.A., and Soranzo, N. (2021). RNA-Seq Data Analysis in Galaxy.
577 Methods Mol Biol *2284*, 367-392.

578 Bissen, D., Kracht, M.K., Foss, F., Hofmann, J., and Acker-Palmer, A. (2021). EphrinB2 and GRIP1
579 stabilize mushroom spines during denervation-induced homeostatic plasticity. Cell Rep *34*, 108923.

580 Chicurel, M.E., and Harris, K.M. (1992). Three-dimensional analysis of the structure and composition
581 of CA3 branched dendritic spines and their synaptic relationships with mossy fiber boutons in the rat
582 hippocampus. J Comp Neurol *325*, 169-182.

583 De Bruyckere, E., Simon, R., Nestel, S., Heimrich, B., Katzel, D., Egorov, A.V., Liu, P., Jenkins, N.A.,
584 Copeland, N.G., Schwegler, H., *et al.* (2018). Stability and Function of Hippocampal Mossy Fiber
585 Synapses Depend on Bcl11b/Ctip2. Front Mol Neurosci *11*, 103.

586 Del Turco, D., and Deller, T. (2007). Organotypic entorhino-hippocampal slice cultures--a tool to study
587 the molecular and cellular regulation of axonal regeneration and collateral sprouting in vitro. Methods
588 Mol Biol *399*, 55-66.

589 Deller, T., Korte, M., Chabanis, S., Drakew, A., Schwegler, H., Stefani, G.G., Zuniga, A., Schwarz, K.,
590 Bonhoeffer, T., Zeller, R., *et al.* (2003). Synaptopodin-deficient mice lack a spine apparatus and show
591 deficits in synaptic plasticity. Proc Natl Acad Sci U S A *100*, 10494-10499.

592 Dubes, S., Soula, A., Benquet, S., Tessier, B., Poujol, C., Favereaux, A., Thoumine, O., and Letellier,
593 M. (2022). miR-124-dependent tagging of synapses by synaptopodin enables input-specific homeostatic
594 plasticity. EMBO J, e109012.

595 Eichler, A., Kleidonas, D., Turi, Z., Fliegauf, M., Kirsch, M., Pfeifer, D., Masuda, T., Prinz, M., Lenz,
596 M., and Vlachos, A. (2022). Microglia mediate synaptic plasticity induced by 10 Hz repetitive
597 transcranial magnetic stimulation. bioRxiv.

598 Falahati, H., Wu, Y., Feuerer, V., Simon, H.G., and De Camilli, P. (2022). Proximity proteomics of
599 synaptopodin provides insight into the molecular composition of the spine apparatus of dendritic spines.
600 Proc Natl Acad Sci U S A *119*, e2203750119.

601 Frotscher, M., and Heimrich, B. (1995). Lamina-specific synaptic connections of hippocampal neurons
602 in vitro. J Neurobiol *26*, 350-359.

603 Frotscher, M., Heimrich, B., and Deller, T. (1997). Sprouting in the hippocampus is layer-specific.
604 Trends Neurosci *20*, 218-223.

605 Frotscher, M., Heimrich, B., Deller, T., and Nitsch, R. (1995). Understanding the cortex through the
606 hippocampus: lamina-specific connections of the rat hippocampal neurons. J Anat *187 (Pt 3)*, 539-545.

607 Galaxy, C. (2022). The Galaxy platform for accessible, reproducible and collaborative biomedical
608 analyses: 2022 update. Nucleic Acids Res.

609 Goecks, J., Nekrutenko, A., Taylor, J., and Galaxy, T. (2010). Galaxy: a comprehensive approach for
610 supporting accessible, reproducible, and transparent computational research in the life sciences.
611 Genome Biol *11*, R86.

612 Gundlfinger, A., Leibold, C., Gebert, K., Moisel, M., Schmitz, D., and Kempter, R. (2007). Differential
613 modulation of short-term synaptic dynamics by long-term potentiation at mouse hippocampal mossy
614 fibre synapses. J Physiol *585*, 853-865.

615 Haber, M., Zhou, L., and Murai, K.K. (2006). Cooperative astrocyte and dendritic spine dynamics at
616 hippocampal excitatory synapses. J Neurosci *26*, 8881-8891.

617 Heller, J.P., and Rusakov, D.A. (2017). The Nanoworld of the Tripartite Synapse: Insights from Super-
618 Resolution Microscopy. Front Cell Neurosci *11*, 374.

619 Hengen, K.B., Lambo, M.E., Van Hooser, S.D., Katz, D.B., and Turrigiano, G.G. (2013). Firing rate
620 homeostasis in visual cortex of freely behaving rodents. Neuron *80*, 335-342.

621 Henze, D.A., McMahon, D.B., Harris, K.M., and Barrionuevo, G. (2002a). Giant miniature EPSCs at
622 the hippocampal mossy fiber to CA3 pyramidal cell synapse are monoquantal. J Neurophysiol *87*, 15-
623 29.

624 Henze, D.A., Wittner, L., and Buzsaki, G. (2002b). Single granule cells reliably discharge targets in the
625 hippocampal CA3 network in vivo. Nat Neurosci *5*, 790-795.

626 Hulme, S.R., Jones, O.D., Raymond, C.R., Sah, P., and Abraham, W.C. (2014). Mechanisms of
627 heterosynaptic metaplasticity. Philos Trans R Soc Lond B Biol Sci *369*, 20130148.

628 Hunsaker, M.R., Rosenberg, J.S., and Kesner, R.P. (2008). The role of the dentate gyrus, CA3a,b, and
629 CA3c for detecting spatial and environmental novelty. Hippocampus *18*, 1064-1073.

630 Jedlicka, P., and Deller, T. (2017). Understanding the role of synaptopodin and the spine apparatus in
631 Hebbian synaptic plasticity - New perspectives and the need for computational modeling. Neurobiol
632 Learn Mem *138*, 21-30.

633 Jedlicka, P., Schwarzacher, S.W., Winkels, R., Kienzler, F., Frotscher, M., Bramham, C.R., Schultz, C.,
634 Bas Orth, C., and Deller, T. (2009). Impairment of in vivo theta-burst long-term potentiation and
635 network excitability in the dentate gyrus of synaptopodin-deficient mice lacking the spine apparatus and
636 the cisternal organelle. Hippocampus *19*, 130-140.

637 Korkotian, E., Frotscher, M., and Segal, M. (2014). Synaptopodin regulates spine plasticity: mediation
638 by calcium stores. J Neurosci *34*, 11641-11651.

639 Lambo, M.E., and Turrigiano, G.G. (2013). Synaptic and intrinsic homeostatic mechanisms cooperate
640 to increase L2/3 pyramidal neuron excitability during a late phase of critical period plasticity. J Neurosci
641 *33*, 8810-8819.

642 Lee, K.J., Queenan, B.N., Rozeboom, A.M., Bellmore, R., Lim, S.T., Vicini, S., and Pak, D.T. (2013).
643 Mossy fiber-CA3 synapses mediate homeostatic plasticity in mature hippocampal neurons. Neuron *77*,
644 99-114.

645 Lenz, M., Eichler, A., Kruse, P., Muellerleile, J., Deller, T., Jedlicka, P., and Vlachos, A. (2021a). All-
646 trans retinoic acid induces synaptopodin-dependent metaplasticity in mouse dentate granule cells. Elife
647 *10*.

648 Lenz, M., Galanis, C., Kleidonas, D., Fellenz, M., Deller, T., and Vlachos, A. (2019). Denervated mouse
649 dentate granule cells adjust their excitatory but not inhibitory synapses following in vitro entorhinal
650 cortex lesion. Exp Neurol *312*, 1-9.

651 Lenz, M., Kruse, P., Eichler, A., Straehle, J., Beck, J., Deller, T., and Vlachos, A. (2021b). All-trans
652 retinoic acid induces synaptic plasticity in human cortical neurons. Elife *10*.

653 Leutgeb, J.K., Leutgeb, S., Moser, M.B., and Moser, E.I. (2007). Pattern separation in the dentate gyrus
654 and CA3 of the hippocampus. Science *315*, 961-966.

655 Lipp, H.P., Schwegler, H., Heimrich, B., and Driscoll, P. (1988). Infrapyramidal mossy fibers and two-
656 way avoidance learning: developmental modification of hippocampal circuitry and adult behavior of
657 rats and mice. J Neurosci *8*, 1905-1921.

658 Maggio, N., and Vlachos, A. (2018). Tumor necrosis factor (TNF) modulates synaptic plasticity in a
659 concentration-dependent manner through intracellular calcium stores. J Mol Med (Berl) *96*, 1039-1047.

660 Marr, D. (1971). Simple memory: a theory for archicortex. Philos Trans R Soc Lond B Biol Sci *262*,
661 23-81.

662 Maus, L., Lee, C., Altas, B., Sertel, S.M., Weyand, K., Rizzoli, S.O., Rhee, J., Brose, N., Imig, C., and
663 Cooper, B.H. (2020). Ultrastructural Correlates of Presynaptic Functional Heterogeneity in
664 Hippocampal Synapses. Cell Rep *30*, 3632-3643 e3638.

Mesulam, M.M., Lalehzari, N., Rahmani, F., Ohm, D., Shahidehpour, R., Kim, G., Gefen, T., Weintraub, S., Bigio, E., and Geula, C. (2019). Cortical cholinergic denervation in primary progressive aphasia with Alzheimer pathology. Neurology *92*, e1580-e1588.

Monday, H.R., Kharod, S.C., Yoon, Y.J., Singer, R.H., and Castillo, P.E. (2022). Presynaptic FMRP and local protein synthesis support structural and functional plasticity of glutamatergic axon terminals. Neuron *110*, 2588-2606 e2586.

Mootha, V.K., Lindgren, C.M., Eriksson, K.F., Subramanian, A., Sihag, S., Lehar, J., Puigserver, P., Carlsson, E., Ridderstrale, M., Laurila, E.*, et al.* (2003). PGC-1alpha-responsive genes involved in oxidative phosphorylation are coordinately downregulated in human diabetes. Nat Genet *34*, 267-273.

O'Reilly, R.C., and McClelland, J.L. (1994). Hippocampal conjunctive encoding, storage, and recall: avoiding a trade-off. Hippocampus *4*, 661-682.

Orlando, M., Dvorzhak, A., Bruentgens, F., Maglione, M., Rost, B.R., Sigrist, S.J., Breustedt, J., and Schmitz, D. (2021). Recruitment of release sites underlies chemical presynaptic potentiation at hippocampal mossy fiber boutons. PLoS Biol *19*, e3001149.

Platschek, S., Cuntz, H., Vuksic, M., Deller, T., and Jedlicka, P. (2016). A general homeostatic principle following lesion induced dendritic remodeling. Acta Neuropathol Commun *4*, 19.

Prang, P., Del Turco, D., and Deller, T. (2003). Associational sprouting in the mouse fascia dentata after entorhinal lesion in vitro. Brain Res *978*, 205-212.

Prince, L.Y., Bacon, T.J., Tigaret, C.M., and Mellor, J.R. (2016). Neuromodulation of the Feedforward Dentate Gyrus-CA3 Microcircuit. Front Synaptic Neurosci *8*, 32.

Reimand, J., Isserlin, R., Voisin, V., Kucera, M., Tannus-Lopes, C., Rostamianfar, A., Wadi, L., Meyer, M., Wong, J., Xu, C.*, et al.* (2019). Pathway enrichment analysis and visualization of omics data using g:Profiler, GSEA, Cytoscape and EnrichmentMap. Nat Protoc *14*, 482-517.

Robinson, J.L., Molina-Porcel, L., Corrada, M.M., Raible, K., Lee, E.B., Lee, V.M., Kawas, C.H., and Trojanowski, J.Q. (2014). Perforant path synaptic loss correlates with cognitive impairment and Alzheimer's disease in the oldest-old. Brain *137*, 2578-2587.

Shannon, P., Markiel, A., Ozier, O., Baliga, N.S., Wang, J.T., Ramage, D., Amin, N., Schwikowski, B., and Ideker, T. (2003). Cytoscape: a software environment for integrated models of biomolecular interaction networks. Genome Res *13*, 2498-2504.

Strehl, A., Galanis, C., Radic, T., Schwarzacher, S.W., Deller, T., and Vlachos, A. (2018). Dopamine Modulates Homeostatic Excitatory Synaptic Plasticity of Immature Dentate Granule Cells in Entorhino-Hippocampal Slice Cultures. Front Mol Neurosci *11*, 303.

Strehl, A., Lenz, M., Itsekson-Hayosh, Z., Becker, D., Chapman, J., Deller, T., Maggio, N., and Vlachos, A. (2014). Systemic inflammation is associated with a reduction in Synaptopodin expression in the mouse hippocampus. Exp Neurol *261*, 230-235.

Subramanian, A., Tamayo, P., Mootha, V.K., Mukherjee, S., Ebert, B.L., Gillette, M.A., Paulovich, A., Pomeroy, S.L., Golub, T.R., Lander, E.S.*, et al.* (2005). Gene set enrichment analysis: a knowledge-based approach for interpreting genome-wide expression profiles. Proc Natl Acad Sci U S A *102*, 15545-15550.

Sutton, M.A., Ito, H.T., Cressy, P., Kempf, C., Woo, J.C., and Schuman, E.M. (2006). Miniature neurotransmission stabilizes synaptic function via tonic suppression of local dendritic protein synthesis. Cell *125*, 785-799.

Thal, D.R., Holzer, M., Rub, U., Waldmann, G., Gunzel, S., Zedlick, D., and Schober, R. (2000). Alzheimer-related tau-pathology in the perforant path target zone and in the hippocampal stratum oriens and radiatum correlates with onset and degree of dementia. Exp Neurol *163*, 98-110.

Turrigiano, G. (2012). Homeostatic synaptic plasticity: local and global mechanisms for stabilizing neuronal function. Cold Spring Harb Perspect Biol *4*, a005736.

Turrigiano, G.G. (2017). The dialectic of Hebb and homeostasis. Philos Trans R Soc Lond B Biol Sci *372*.

714 Turrigiano, G.G., Leslie, K.R., Desai, N.S., Rutherford, L.C., and Nelson, S.B. (1998). Activity-
715 dependent scaling of quantal amplitude in neocortical neurons. Nature *391*, 892-896.

716 Vandael, D., Borges-Merjane, C., Zhang, X., and Jonas, P. (2020). Short-Term Plasticity at
717 Hippocampal Mossy Fiber Synapses Is Induced by Natural Activity Patterns and Associated with
718 Vesicle Pool Engram Formation. Neuron *107*, 509-521 e507.

719 Vandael, D., Okamoto, Y., Borges-Merjane, C., Vargas-Barroso, V., Suter, B.A., and Jonas, P. (2021a).
720 Subcellular patch-clamp techniques for single-bouton stimulation and simultaneous pre- and
721 postsynaptic recording at cortical synapses. Nat Protoc *16*, 2947-2967.

722 Vandael, D., Okamoto, Y., and Jonas, P. (2021b). Transsynaptic modulation of presynaptic short-term
723 plasticity in hippocampal mossy fiber synapses. Nat Commun *12*, 2912.

724 Viana da Silva, S., Zhang, P., Haberl, M.G., Labrousse, V., Grosjean, N., Blanchet, C., Frick, A., and
725 Mulle, C. (2019). Hippocampal Mossy Fibers Synapses in CA3 Pyramidal Cells Are Altered at an Early
726 Stage in a Mouse Model of Alzheimer's Disease. J Neurosci *39*, 4193-4205.

727 Villanueva-Castillo, C., Tecuatl, C., Herrera-Lopez, G., and Galvan, E.J. (2017). Aging-related
728 impairments of hippocampal mossy fibers synapses on CA3 pyramidal cells. Neurobiol Aging *49*, 119-
729 137.

730 Vitureira, N., Letellier, M., and Goda, Y. (2012). Homeostatic synaptic plasticity: from single synapses
731 to neural circuits. Curr Opin Neurobiol *22*, 516-521.

732 Vlachos, A. (2012). Synaptopodin and the spine apparatus organelle-regulators of different forms of
733 synaptic plasticity? Ann Anat *194*, 317-320.

734 Vlachos, A., Bas Orth, C., Schneider, G., and Deller, T. (2012a). Time-lapse imaging of granule cells
735 in mouse entorhino-hippocampal slice cultures reveals changes in spine stability after entorhinal
736 denervation. J Comp Neurol *520*, 1891-1902.

737 Vlachos, A., Becker, D., Jedlicka, P., Winkels, R., Roeper, J., and Deller, T. (2012b). Entorhinal
738 denervation induces homeostatic synaptic scaling of excitatory postsynapses of dentate granule cells in
739 mouse organotypic slice cultures. PLoS One *7*, e32883.

740 Vlachos, A., Ikenberg, B., Lenz, M., Becker, D., Reifenberg, K., Bas-Orth, C., and Deller, T. (2013).
741 Synaptopodin regulates denervation-induced homeostatic synaptic plasticity. Proc Natl Acad Sci U S A
742 *110*, 8242-8247.

743 Vlachos, A., Korkotian, E., Schonfeld, E., Copanaki, E., Deller, T., and Segal, M. (2009). Synaptopodin
744 regulates plasticity of dendritic spines in hippocampal neurons. J Neurosci *29*, 1017-1033.

745 Vyleta, N.P., Borges-Merjane, C., and Jonas, P. (2016). Plasticity-dependent, full detonation at
746 hippocampal mossy fiber-CA3 pyramidal neuron synapses. Elife *5*.

747 Vyleta, N.P., and Jonas, P. (2014). Loose coupling between Ca2+ channels and release sensors at a
748 plastic hippocampal synapse. Science *343*, 665-670.

749 Weng, F.J., Garcia, R.I., Lutzu, S., Alvina, K., Zhang, Y., Dushko, M., Ku, T., Zemoura, K., Rich, D.,
750 Garcia-Dominguez, D.*, et al.* (2018). Npas4 Is a Critical Regulator of Learning-Induced Plasticity at
751 Mossy Fiber-CA3 Synapses during Contextual Memory Formation. Neuron *97*, 1137-1152 e1135.

752 Wingo, A.P., Dammer, E.B., Breen, M.S., Logsdon, B.A., Duong, D.M., Troncosco, J.C., Thambisetty,
753 M., Beach, T.G., Serrano, G.E., Reiman, E.M.*, et al.* (2019). Large-scale proteomic analysis of human
754 brain identifies proteins associated with cognitive trajectory in advanced age. Nat Commun *10*, 1619.

755 Wu, C.H., Tatavarty, V., Jean Beltran, P.M., Guerrero, A.A., Keshishian, H., Krug, K., MacMullan,
756 M.A., Li, L., Carr, S.A., Cottrell, J.R.*, et al.* (2022). A bidirectional switch in the Shank3
757 phosphorylation state biases synapses toward up- or downscaling. Elife *11*.

758 Yap, K., Drakew, A., Smilovic, D., Rietsche, M., Paul, M.H., Vuksic, M., Del Turco, D., and Deller, T.
759 (2020). The actin-modulating protein synaptopodin mediates long-term survival of dendritic spines.
760 Elife *9*.

761 Zalutsky, R.A., and Nicoll, R.A. (1990). Comparison of two forms of long-term potentiation in single
762 hippocampal neurons. Science *248*, 1619-1624.

763

764 **FIGURES**

765 **Figure 1: Entorhinal cortex lesion causes homeostatic synaptic plasticity in both dentate granule**
766 **cells and CA3 pyramidal cells.**

767 (A) Entorhinal cortex lesion (ECL) in organotypic entorhino-hippocampal tissue cultures was
768 performed by dissecting the perforant path (white line, scale bar 300 µm). Hippocampal cells were
769 visualized by post-hoc staining of neurons after electrophysiological assessment.

770 (B) Spontaneous excitatory postsynaptic currents (sEPSCs) were recorded in both dentate granule cells
771 and CA3 pyramidal cells in non-lesioned and lesioned cultures (3 days post lesion, 3 dp ECL).

772 (C-D) Spontaneous EPSC analysis in dentate granule cells reveals a lesion-induced excitatory synaptic
773 strengthening in the mean sEPSC amplitude, half width and area (C; $n_{control}$ = 22 cells; $n_{3dp\ ECL}$ = 22 cells;
774 Mann-Whitney test; Linear regression fit for XY-plot analysis). Percentile analysis of sEPSC
775 amplitudes (D) demonstrates that the excitatory synaptic strengthening is detected in the 50% largest
776 events (Mann-Whitney test).

777 (E-F) The frequency of sEPSCs is significantly increased 3 days after ECL (E; Mann-Whitney test).
778 Moreover, amplitude/frequency-analysis shows that the abundance of larger sEPSC amplitudes is higher
779 in lesioned cultures when compared to non-lesioned controls (F; RM-two-way ANOVA followed by
780 Sidak's multiple comparisons test).

781 (G-H) Spontaneous EPSC analysis in CA3 pyramidal cells reveals a lesion-induced increase in mean
782 sEPSC amplitude, whereas half width and area remained unchanged (G; $n_{control}$ = 48 cells; $n_{3dp\ ECL}$ = 49
783 cells; Mann-Whitney test; Linear regression fit for XY-plot analysis). Percentile analysis of sEPSC
784 amplitudes (H) demonstrates that the excitatory synaptic strengthening is only visible in the 50% largest
785 events (Mann-Whitney test).

786 (I-J) No lesion-induced changes in mean sEPSC frequency was detectable in CA3 pyramidal neurons.
787 Amplitude/frequency-analysis shows a reduced portion of smaller events in CA3 pyramidal cells 3 days
788 after ECL (Mann-Whitney test for column statistics and RM-two-way ANOVA followed by Sidak's
789 multiple comparisons test for XY-plot analysis).

790 Individual data points are indicated by colored dots. Values represent mean ± s.e.m (*$p < 0.05$, **$p <$
791 0.01, ***$p < 0.001$, ns - non significant difference).

Figure 2: Lesion-induced loss of the cortico-hippocampal projection leads to changed transmission at hippocampal mossy fiber synapses.

(A) Post-hoc visualization of patched neurons in organotypic tissue cultures after paired-electrophysiological recordings between individual presynaptic (pre) dentate granule cells and postsynaptic (post) CA3 pyramidal neurons to analyze synaptic transmission features at hippocampal mossy fiber synapses (scale bar 300 µm).

(B) Five consecutive action potentials were induced in dentate granule cells at 20 Hz (bottom trace) to assess postsynaptic responses in CA3 pyramidal neurons in lesioned and non-lesioned control cultures (upper traces).

(C) The response rate, i.e., the fraction of presynaptic pulses that elicited a postsynaptic response in a connected pair of individual neurons, was significantly increased for the first two pulses in lesioned cultures when compared to non-lesioned controls ($n_{control} = 10$; $n_{3dp\ ECL} = 10$; Mann-Whitney test for the respective pulse numbers).

(D) In successfully elicited unitary EPSCs (uEPSCs), a significant increase in uEPSC amplitude was detectable ($n°1_{control} = 20$ events, $n°1_{ECL} = 187$ events; $n°2_{control} = 115$ events, $n°2_{ECL} = 304$ events; $n°3_{control} = 292$ events, $n°3_{ECL} = 394$ events (one data point outside the axis limits); $n°4_{control} = 326$ events, $n°4_{ECL} = 385$ events; $n°5_{control} = 307$ events, $n°5_{ECL} = 384$ events; Mann-Whitney test for the respective pulse numbers).

Individual data points are indicated by colored dots. Values represent mean ± s.e.m (*$p < 0.05$, **$p < 0.01$, ***$p < 0.001$, ns - non significant difference).

Figure 3: The spine apparatus organelle is a hub for ribosomes and excitatory synapse related mRNAs.

(A) Transmission electron microscopy (TEM) images suggest a close association of ribosomes (arrowheads) and the spine apparatus organelle. Scale bar = 300 nm.

(B) Bioanalyzer traces (picoRNA Chip) from RNA samples prepared from precleared input (left) and Synpo-coIPs (right). Traces demonstrate the co-immunoprecipitation of ribosomal RNA with anti-synaptopodin antibody. Notably, beads-only controls did not show an immunoprecipitation of rRNA.

(C) RT-qPCR analysis demonstrates a significant enrichment of Gria1 mRNA in synaptopodin-coIP compared to input samples indicating an association between the spine apparatus organelle and synaptic plasticity related mRNAs (normalized to Gapdh; $n_{input/SP\text{-}coIP} = 10$ samples, Mann-Whitney test).

(D) Analysis of differential mRNA abundance in Synpo-coIP RNA samples compared to their respective input samples to reveal the synaptopodin related transcriptome. A log2(FC) value > 0 indicates an mRNA enrichment in Synpo-coIP samples (UP: 2355 genes). Differentially enriched genes ($p_{adj.} < 0.05$) are indicated by orange dots (n = 5 samples input and Synpo-coIP respectively; 5-6 tissue cultures pooled from one filter per sample; DESeq2-analysis, usegalaxy.eu platform).

(E) A gene set enrichment analysis for a cellular compartment gene ontology was performed for significantly enriched genes in Synpo-coIP samples and visualized by a cytoscape map (node cutoff p = 0.05, edge cutoff (similarity): 0.8; node size represents gene set size; node positions have been manually adjusted).

(F) Transmission electron microscopy was used to visualize ultrastructural properties of mossy fiber synapses in lesioned and non-lesioned control cultures (scale bar 1 µm).

(G) Upon lesion, the abundance of spine apparatus organelles (SA) and their number of dense plates were significantly increased in the postsynaptic compartment of mossy fiber synapses ($n_{control} = 120$ (no SA = 97 postsynapses, 1 dense plate = 22 postsynapses, 2 dense plates = 1 postsynapse, 3 dense plates = 0 postsynapses); $n_{ECL} = 90$ (no SA = 56 postsynapses, 1 dense plate = 21 postsynapses, 2 dense plates = 12 postsynapses, 3 dense plates = 1 postsynapses)).

(H) While the number of dense plates increased, their length significantly decreased 3 days after ECL ($n_{control} = 24$ (one data point outside the axis limits; $n_{ECL} = 48$, Mann-Whitney test).

Individual data points are indicated by colored dots. Values represent mean ± s.e.m (*p < 0.05, **p < 0.01, ns - non significant difference).

842 **Figure 4: Lesion-induced homeostatic synaptic plasticity at hippocampal mossy fiber synapses is**
843 **impaired in synaptopodin-deficient mice.**
844 (A-B) sEPSCs were recorded from dentate granule cells in synaptopodin-deficient tissue cultures
845 (Synpo$^{-/-}$). Here, the mean sEPSC amplitude, half width and area significantly increased 3 days after the
846 ECL (A; $n_{control}$ = 29; $n_{3dp\ ECL}$ = 26; Mann-Whitney test; Linear regression fit for XY-plot analysis). In
847 contrast to wildtype cultures, no changes in the mean sEPSC frequency or the sEPSC
848 amplitude/frequency-distribution were observed (B; Mann-Whitney test for column statistics and RM-
849 two-way ANOVA followed by Sidak's multiple comparisons test for XY-plot analysis).
850 (C) No changes in passive membrane properties of dentate granule cells were detected in synaptopodin-
851 deficient cultures upon lesion (Mann-Whitney test for column statistics and RM-two-way ANOVA
852 followed by Sidak's multiple comparisons test for XY-plot analysis).
853 (D-E) The mean sEPSC amplitude in CA3 pyramidal neurons was not significantly different in lesioned
854 and non-lesioned control cultures. Noteworthy, the mean sEPSC half width significantly decreased in
855 lesioned cultures (D; $n_{control}$ = 25; $n_{3dp\ ECL}$ = 25; Mann-Whitney test; linear regression fit for XY-plot
856 analysis). No lesion-induced changes in the mean sEPSC frequency or the amplitude/frequency-
857 interdependence were detectable (E; Mann-Whitney test for column statistics and RM-two-way
858 ANOVA followed by Sidak's multiple comparisons test for XY-plot analysis).
859 (F) No changes in passive membrane properties of CA3 pyramidal neurons were detected in
860 synaptopodin-deficient cultures upon lesion (Mann-Whitney test for column statistics and RM-two-way
861 ANOVA followed by Sidak's multiple comparisons test for XY-plot analysis).
862 (G-H) Paired whole-cell patch-clamp recordings were carried out between individual dentate granule
863 cells (GC) and CA3 pyramidal neurons in lesioned and non-lesioned control cultures prepared from
864 synaptopodin-deficient animals (G). Upon injection of 5 presynaptic current pulses in the presynaptic
865 granule cells, no changes in the pulse-number-dependent response rate of connected mossy fiber
866 synapses were detectable after the ECL (H; $n_{control}$ = 12; $n_{3dp\ ECL}$ = 10; Mann-Whitney test for the
867 respective pulse numbers).
868 (I) Analyzing properties of successfully transmitted uEPSCs, a significant decrease in uEPSC amplitude
869 was evident in lesioned cultures when compared to non-lesioned controls ($n°1_{control}$ = 144 events, $n°1_{ECL}$
870 = 82 events; $n°2_{control}$ = 300 events, $n°2_{ECL}$ = 263 events; $n°3_{control}$ = 426 events (one data point outside
871 the axis limits), $n°3_{ECL}$ = 402 events; $n°4_{control}$ = 486 events, $n°4_{ECL}$ = 364 events; $n°5_{control}$ = 472 events,
872 $n°5_{ECL}$ = 317 events; Mann-Whitney test for the respective pulse numbers).
873 Individual data points are indicated by colored dots. Values represent mean ± s.e.m (*$p < 0.05$, ***$p <$
874 0.001, ns - non significant difference).

875 **Figure 5: Entorhinal cortex lesion leads to synaptopodin-dependent transcriptomic changes in the**
876 **CA3 area of organotypic tissue cultures.**
877 (A) Volcano Plots to visualize differential gene expression in wildtype (Synpo$^{+/+}$) and synaptopodin-
878 deficient (Synpo$^{-/-}$) tissue preparations based on region-specific transcriptome analysis of the dentate
879 gyrus and the CA3 area. Red dots indicate differentially expressed genes ($p_{adj.} < 0.05$; CA3-Synpo$^{+/+}$:
880 $n_{control} = 2$, $n_{3dpECL} = 3$; DG-Synpo$^{+/+}$: $n_{control} = 4$, $n_{3dpECL} = 7$; CA3-Synpo$^{-/-}$: $n_{control} = 6$, $n_{3dpECL} = 6$; DG-
881 Synpo$^{-/-}$: $n_{control} = 7$, $n_{3dpECL} = 4$).
882 (B) VENN-Diagrams illustrate the magnitude of lesion-induced differential gene expression and the
883 overlap in commonly regulated genes between wildtype and synaptopodin-deficient tissue preparations.
884 The illustration indicates that (1) synaptopodin-deficient preparations show deficits in lesion-driven
885 gene expression mainly in CA3 and (2) despite the identification of commonly regulated genes, a
886 considerable number of genotype-specific genes can be identified.
887 (C) For wildtype cultures (Synpo$^{+/+}$), a gene set enrichment analysis was performed and visualized by
888 cytoscape maps and enrichment plots for both hippocampal regions. In both regions, a transcriptional
889 inflammatory response that is accompanied by metabolic changes, can be detected.
890 (D) To identify differentially expressed genes that relate to synaptic transmission in wildtype cultures
891 (Synpo$^{+/+}$), DESeq2-output was filtered for genes listed in the cellular compartment genes ontology
892 "synapse" (GOCC: 0045202). Heatmap-visualization demonstrate that the expression of synapse
893 related genes is a target for lesion-induced cellular remodeling.
894 Analysis was performed on the Galaxy platform, Differential gene expression was determined using the
895 DESeq2 application.

896 **Figure S1: Entorhinal cortex lesion does not influence active or passive membrane properties.**
897 (A-B) Both resting membrane potential and input resistance (A) as well as the input-output curve for
898 the first 15 sweeps of current injection (B) in dentate granule cells were unaffected by the ECL ($n_{control}$
899 = 22 cells; $n_{3dp\ ECL}$ = 22 cells; Mann-Whitney test and RM two-way ANOVA followed by Sidak's
900 multiple comparisons test for XY-plot analysis).
901 (C) Action potential frequency upon increasing current injection in dentate granule cells is similar in
902 non-lesioned and lesioned cultures (RM two-way ANOVA followed by Sidak's multiple comparisons
903 test).
904 (D-E) Both resting membrane potential and input resistance (D) as well as the input-output curve for
905 the first 15 sweeps of current injection (E) in CA3 pyramidal neurons were unaffected by the ECL
906 ($n_{control}$ = 48 cells; $n_{3dp\ ECL}$ = 49 cells; Mann-Whitney test and RM two-way ANOVA followed by Sidak's
907 multiple comparisons test for XY-plot analysis).
908 (F) Action potential frequency upon increasing current injection in dentate granule cells is similar in
909 non-lesioned and lesioned cultures (RM two-way ANOVA followed by Sidak's multiple comparisons
910 test).
911 Individual data points are indicated by colored dots. Values represent mean ± s.e.m (ns - non significant
912 difference).

913 **Figure S2: Entorhinal cortex lesion does not promote major changes in synaptopodin-associated**
914 **mRNA.**
915 Volcano plots to visualize the differential abundance of mRNAs in lesioned and non-lesioned cultures.
916 Both input and Synpo-coIP samples have been analyzed. Differentially expressed/enriched genes ($p_{adj.}$
917 < 0.05) are indicated by orange dots (n = 5 samples for both lesioned and non-lesioned cultures; 5-6
918 tissue cultures pooled from one filter per sample; DESeq2-analysis, usegalaxy.eu platform).

Figure S3: Synaptopodin deficiency shifts the hippocampal mossy fiber synapse to an excitable state under baseline conditions.

(A-B) sEPSCs were recorded from CA3 pyramidal cells of both synaptopodin-deficient and wildtype tissue preparations respectively. While the mean sEPSC amplitude remained unchanged, sEPSC area and half width were significantly increased in synaptopodin-deficient tissue cultures (A; $n_{Synpo+/+} = 48$; $n_{Synpo-/-} = 25$; Mann-Whitney test; Linear regression fit for XY-plot analysis). Additionally, the sEPSC amplitude/frequency-distribution was significantly changed between the two groups (B; RM-two-way ANOVA followed by Sidak's multiple comparisons test).

(C-D) When comparing the response rate of postsynaptic CA3 neurons upon presynaptic action potential generation between paired recordings of $Synpo^{+/+}$ and $Synpo^{-/-}$ tissue preparations, no significant increase was observed (C; $n_{Synpo+/+} = 10$; $n_{Synpo-/-} = 12$; Mann-Whitney test for the respective pulse numbers). However, when analyzing the amplitudes of successfully transmitted uEPSCs at the postsynaptic CA3 pyramidal cells, a significant increase in uEPSC amplitudes became evident in synaptopodin-deficient tissue preparations after each of the five pulses respectively (D; $n°1_{Synpo+/+} = 20$ events, $n°1_{Synpo-/-} = 144$ events; $n°2_{Synpo+/+} = 115$ events, $n°2_{Synpo-/-} = 300$ events; $n°3_{Synpo+/+} = 292$ events, $n°3_{Synpo-/-} = 426$ events (one data point outside the axis limits); $n°4_{Synpo+/+} = 326$ events, $n°4_{Synpo-/-} = 486$ events; $n°5_{Synpo+/+} = 307$ events, $n°5_{Synpo-/-} = 472$ events; Mann-Whitney test for the respective pulse numbers).

Individual data points are indicated by colored dots. Values represent mean ± s.e.m (*$p < 0.05$, **$p < 0.01$, ***$p < 0.001$, ns - non significant difference).

939 **SUPPLEMENTARY TABLES**

940 Table S1: DESeq2 results table Synpo-coIP vs. input (BaseMean > 300; c.f. Fig. 3)

941 Table S2: Synpo-coIP enriched genes (log2FC > 0; c.f. Fig. 3)

942 Table S3: DESeq2 results table ECL vs. control (input; Base Mean > 300; c.f. Figure S2)

943 Table S4: DESeq2 results table ECL vs. control (Synpo-coIP; Base Mean > 300; c.f. Figure S2)

944 Table S5: DESeq2 results table ECL vs. control (Synpo$^{+/+}$, CA3; Base Mean > 300; c.f. Figure 5)

945 Table S6: DESeq2 results table ECL vs. control (Synpo$^{+/+}$, DG; Base Mean > 300; c.f. Figure 5)

946 Table S7: DESeq2 results table ECL vs. control (Synpo$^{-/-}$, CA3; Base Mean > 300; c.f. Figure 5)

947 Table S8: DESeq2 results table ECL vs. control (Synpo$^{-/-}$, DG; Base Mean > 300; c.f. Figure 5)

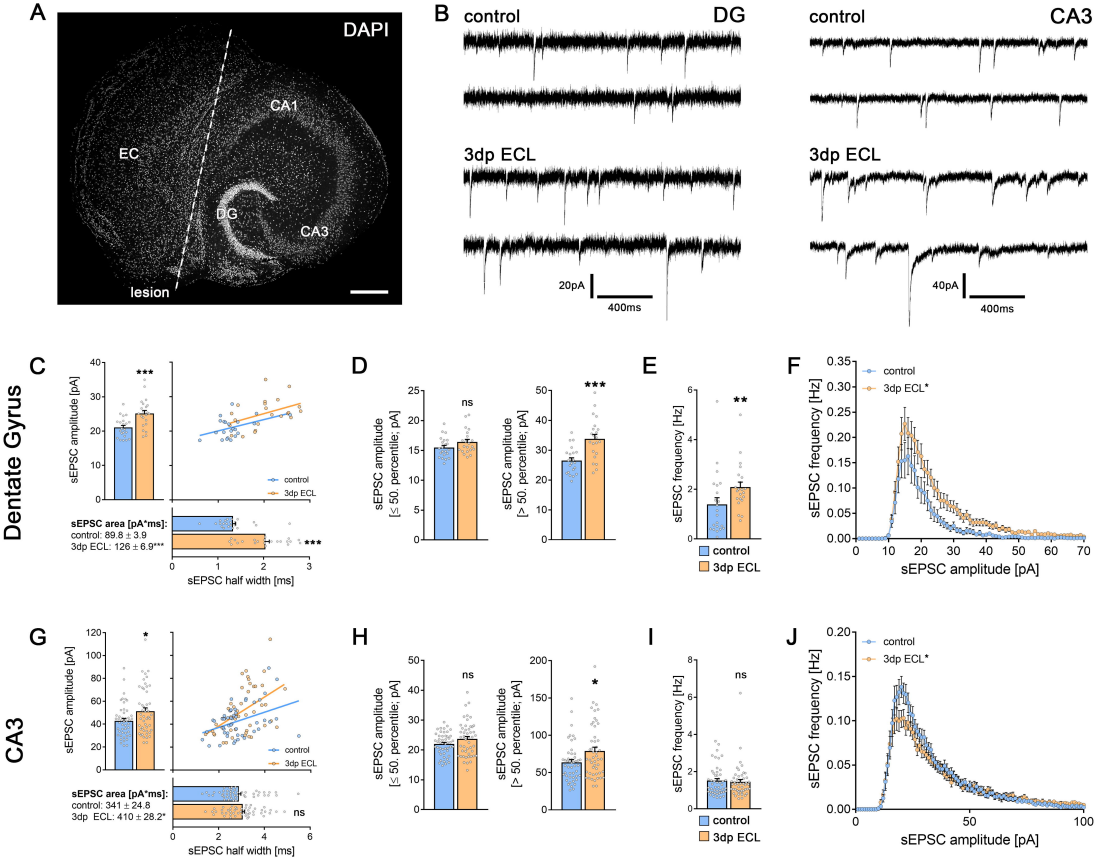
A
DAPI
CA1
EC
DG
CA3
lesion
B
control
DG
3dp ECL
20pA
400ms
control
CA3
3dp ECL
40pA
400ms
Dentate Gyrus
C
sEPSC amplitude [pA]
***
control
3dp ECL
sEPSC area [pA*ms]:
control: 89.8 ± 3.9
3dp ECL: 126 ± 6.9***
***
sEPSC half width [ms]
D
sEPSC amplitude [≤ 50. percentile; pA]
ns
sEPSC amplitude [> 50. percentile; pA]
***
E
sEPSC frequency [Hz]
**
control
3dp ECL
F
sEPSC frequency [Hz]
control
3dp ECL*
sEPSC amplitude [pA]
CA3
G
sEPSC amplitude [pA]
*
control
3dp ECL
sEPSC area [pA*ms]:
control: 341 ± 24.8
3dp ECL: 410 ± 28.2*
ns
sEPSC half width [ms]
H
sEPSC amplitude [≤ 50. percentile; pA]
ns
sEPSC amplitude [> 50. percentile; pA]
*
I
sEPSC frequency [Hz]
ns
control
3dp ECL
J
sEPSC frequency [Hz]
control
3dp ECL*
sEPSC amplitude [pA]

Figure 1

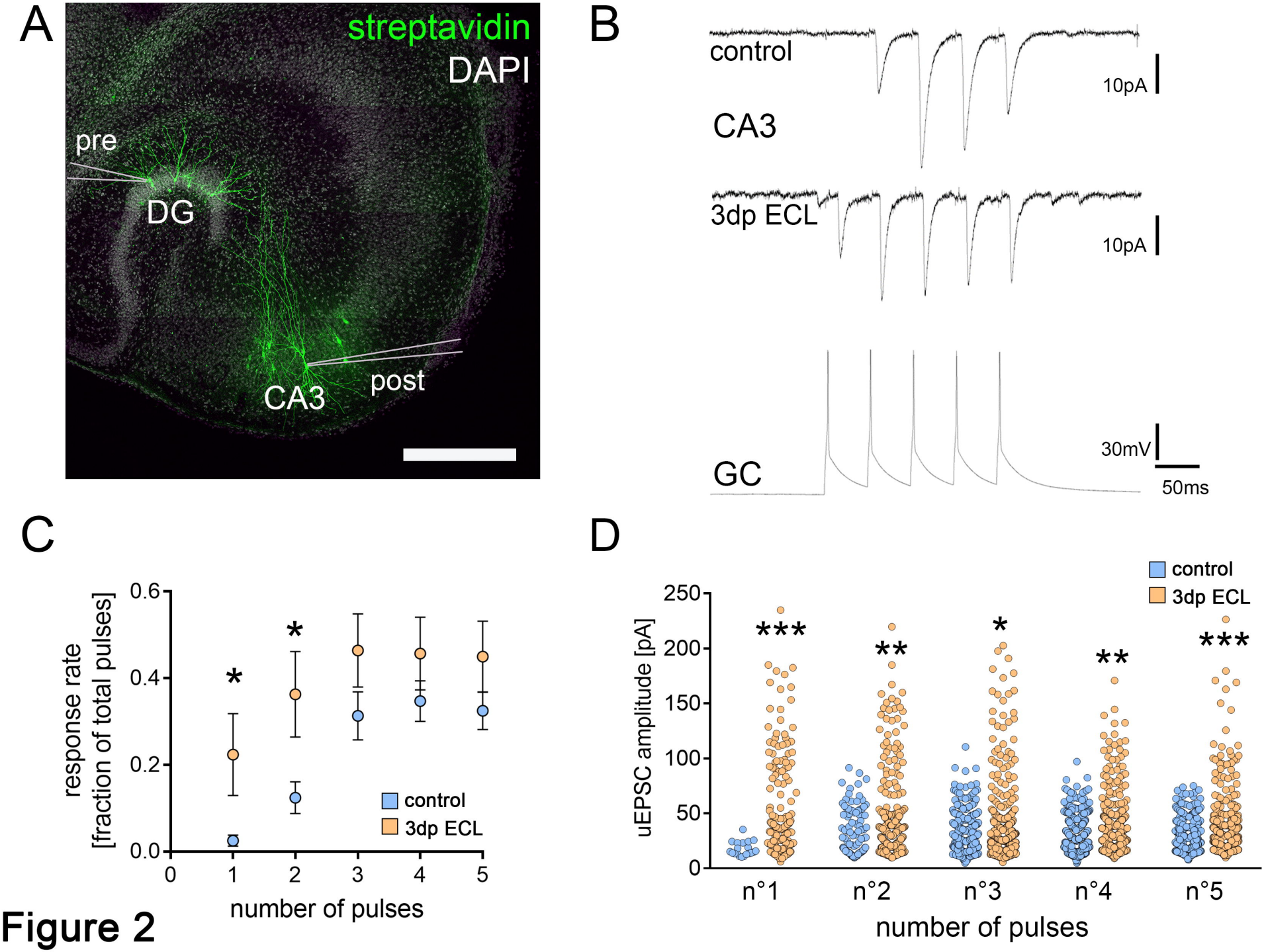
A
streptavidin
DAPI
pre
DG
CA3
post
B
control
10pA
CA3
3dp ECL
10pA
30mV
GC
50ms
C
response rate
[fraction of total pulses]
0.6
0.4
0.2
0.0
0
1
2
3
4
5
number of pulses
control
3dp ECL
D
control
3dp ECL
uEPSC amplitude [pA]
250
200
150
100
50
0
n°1
n°2
n°3
n°4
n°5
number of pulses

Figure 2

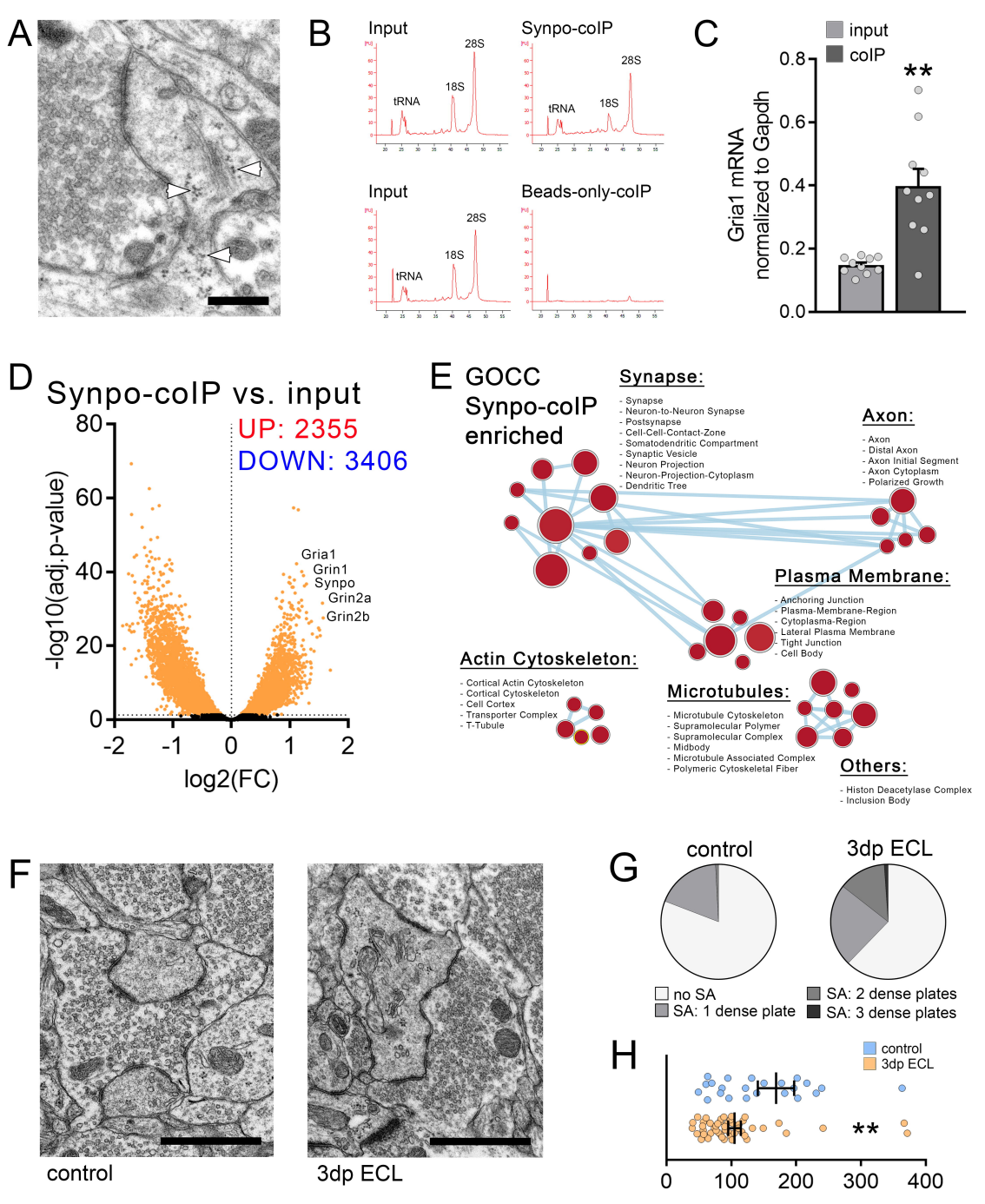
A
B
Input
Synpo-coIP
Input
Beads-only-coIP
tRNA
18S
28S
C
input
coIP
Gria1 mRNA normalized to Gapdh
0.0
0.2
0.4
0.6
0.8
**
D
Synpo-coIP vs. input
UP: 2355
DOWN: 3406
-log10(adj.p-value)
log2(FC)
Gria1
Grin1
Synpo
Grin2a
Grin2b
E
GOCC Synpo-coIP enriched
Synapse:
- Synapse
- Neuron-to-Neuron Synapse
- Postsynapse
- Cell-Cell-Contact-Zone
- Somatodendritic Compartment
- Synaptic Vesicle
- Neuron Projection
- Neuron-Projection-Cytoplasm
- Dendritic Tree
Axon:
- Axon
- Distal Axon
- Axon Initial Segment
- Axon Cytoplasm
- Polarized Growth
Plasma Membrane:
- Anchoring Junction
- Plasma-Membrane-Region
- Cytoplasma-Region
- Lateral Plasma Membrane
- Tight Junction
- Cell Body
Actin Cytoskeleton:
- Cortical Actin Cytoskeleton
- Cortical Cytoskeleton
- Cell Cortex
- Transporter Complex
- T-Tubule
Microtubules:
- Microtubule Cytoskeleton
- Supramolecular Polymer
- Supramolecular Complex
- Midbody
- Microtubule Associated Complex
- Polymeric Cytoskeletal Fiber
Others:
- Histon Deacetylase Complex
- Inclusion Body
F
control
3dp ECL
G
control
3dp ECL
no SA
SA: 1 dense plate
SA: 2 dense plates
SA: 3 dense plates
H
control
3dp ECL
**
0
100
200
300
400
dense plate length [nm]

Figure 3

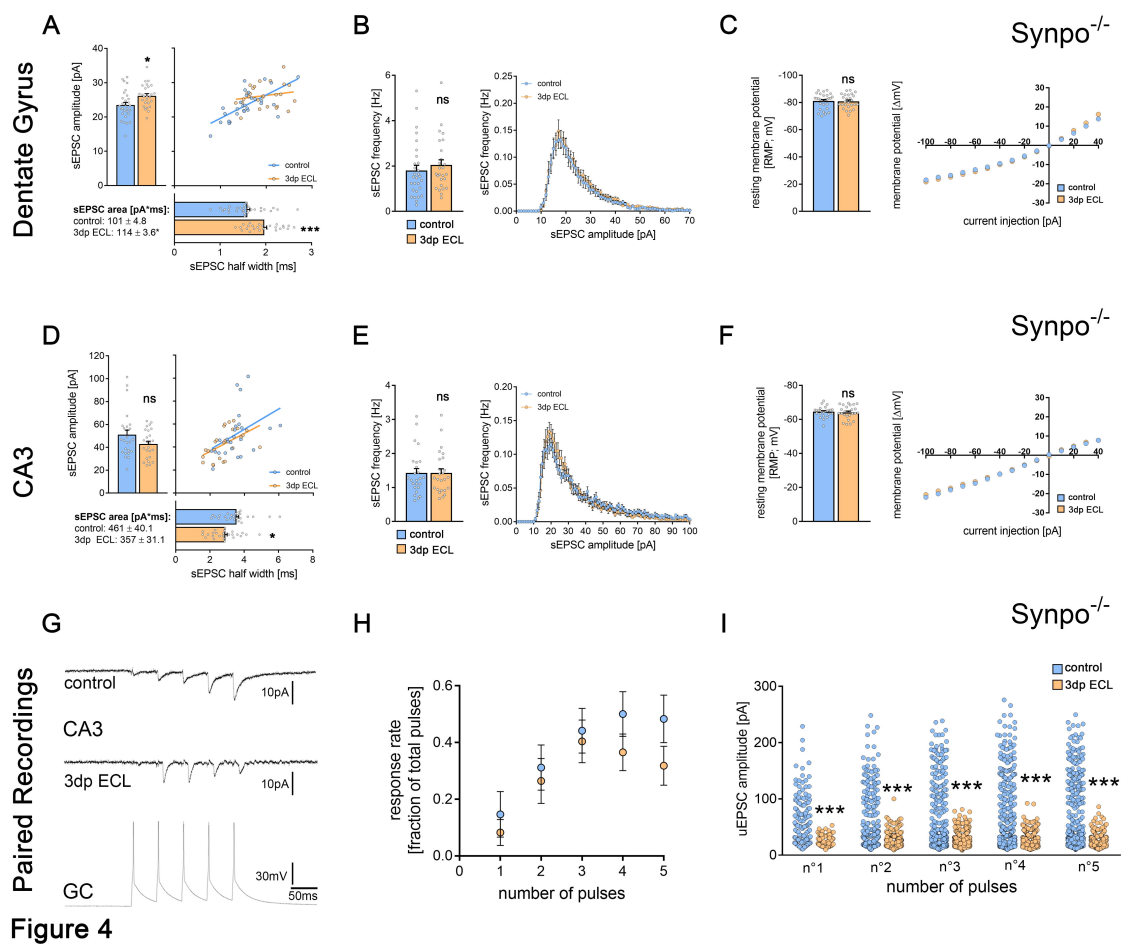
Synpo-/-
Dentate Gyrus
A
sEPSC amplitude [pA]
control
3dp ECL
sEPSC area [pA*ms]:
control: 101 ± 4.8
3dp ECL: 114 ± 3.6*
sEPSC half width [ms]
B
sEPSC frequency [Hz]
ns
control
3dp ECL
sEPSC amplitude [pA]
C
resting membrane potential [RMP; mV]
membrane potential [ΔmV]
current injection [pA]
CA3
D
sEPSC area [pA*ms]:
control: 461 ± 40.1
3dp ECL: 357 ± 31.1
E
F
Paired Recordings
G
control
CA3
3dp ECL
10pA
GC
30mV
50ms
H
response rate [fraction of total pulses]
number of pulses
I
uEPSC amplitude [pA]
n°1
n°2
n°3
n°4
n°5

Figure 4

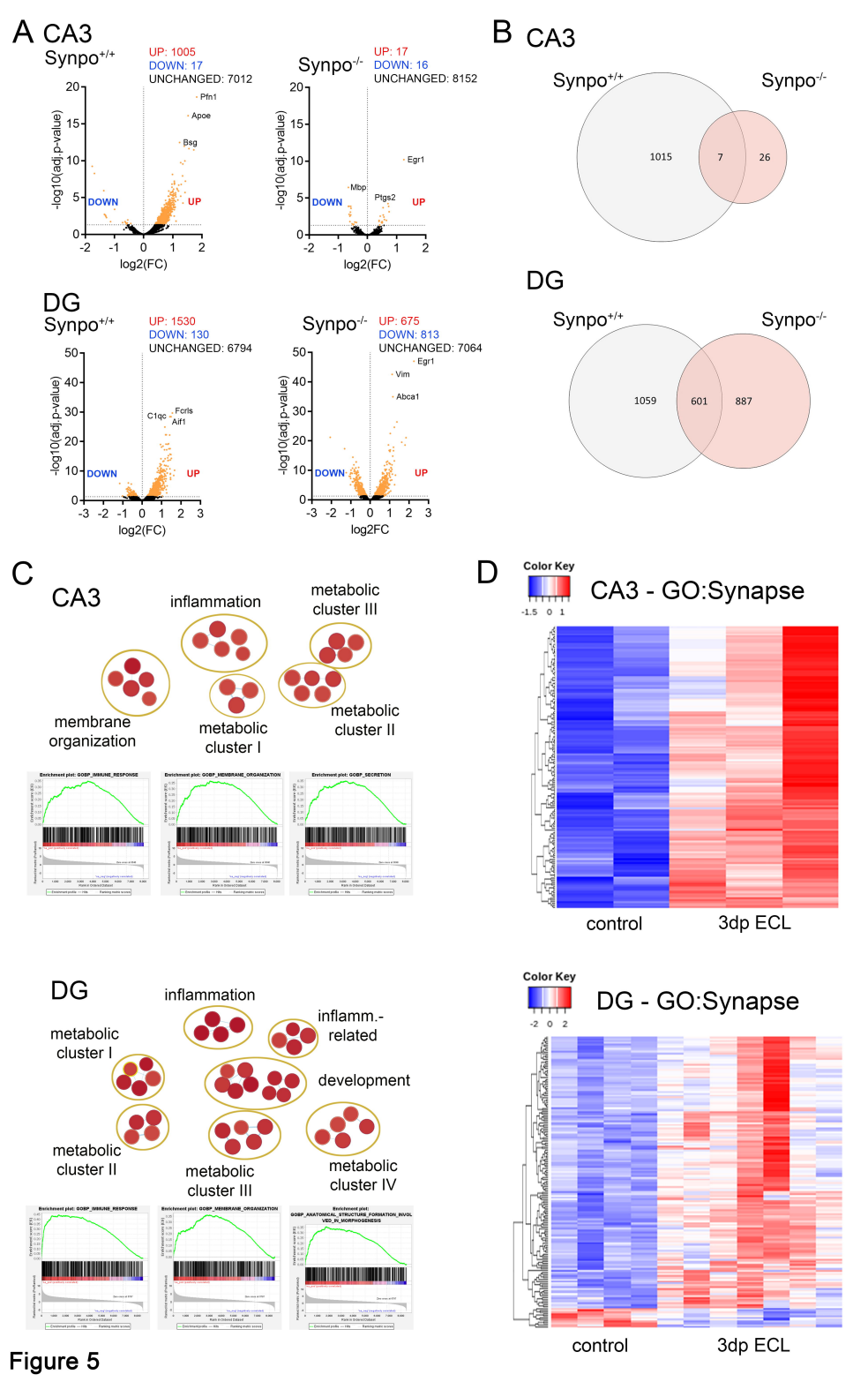
A
CA3
Synpo+/+
UP: 1005
DOWN: 17
UNCHANGED: 7012
Pfn1
Apoe
Bsg
DOWN
UP
-log10(adj.p-value)
log2(FC)
Synpo-/-
UP: 17
DOWN: 16
UNCHANGED: 8152
Egr1
Mbp
Ptgs2
DOWN
UP
-log10(adj.p-value)
log2(FC)
DG
Synpo+/+
UP: 1530
DOWN: 130
UNCHANGED: 6794
C1qc
Fcrls
Aif1
DOWN
UP
-log10(adj.p-value)
log2(FC)
Synpo-/-
UP: 675
DOWN: 813
UNCHANGED: 7064
Egr1
Vim
Abca1
DOWN
UP
-log10(adj.p-value)
log2FC
B
CA3
Synpo+/+
Synpo-/-
1015
7
26
DG
Synpo+/+
Synpo-/-
1059
601
887
C
CA3
inflammation
metabolic cluster III
membrane organization
metabolic cluster I
metabolic cluster II
Enrichment plot: GOBP_IMMUNE_RESPONSE
Enrichment plot: GOBP_MEMBRANE_ORGANIZATION
Enrichment plot: GOBP_SECRETION
DG
inflammation
inflamm.-related
metabolic cluster I
development
metabolic cluster II
metabolic cluster III
metabolic cluster IV
Enrichment plot: GOBP_IMMUNE_RESPONSE
Enrichment plot: GOBP_MEMBRANE_ORGANIZATION
Enrichment plot: GOBP_ANATOMICAL_STRUCTURE_FORMATION_INVOLVED_IN_MORPHOGENESIS
D
Color Key
-1.5 0 1
CA3 - GO:Synapse
control
3dp ECL
Color Key
-2 0 2
DG - GO:Synapse
control
3dp ECL

Figure 5

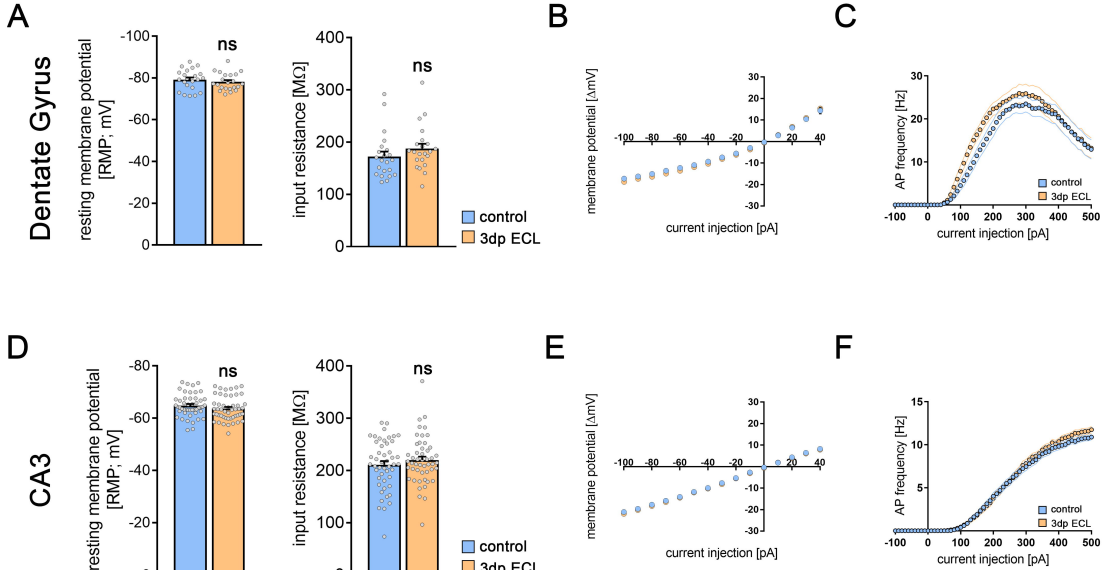
A
Dentate Gyrus
resting membrane potential [RMP; mV]
-100
-80
-60
-40
-20
0
ns
input resistance [MΩ]
400
300
200
100
0
ns
control
3dp ECL
B
membrane potential [ΔmV]
current injection [pA]
C
AP frequency [Hz]
current injection [pA]
control
3dp ECL
D
CA3
resting membrane potential [RMP; mV]
ns
input resistance [MΩ]
ns
control
3dp ECL
E
membrane potential [ΔmV]
current injection [pA]
F
AP frequency [Hz]
current injection [pA]
control
3dp ECL

Figure S1

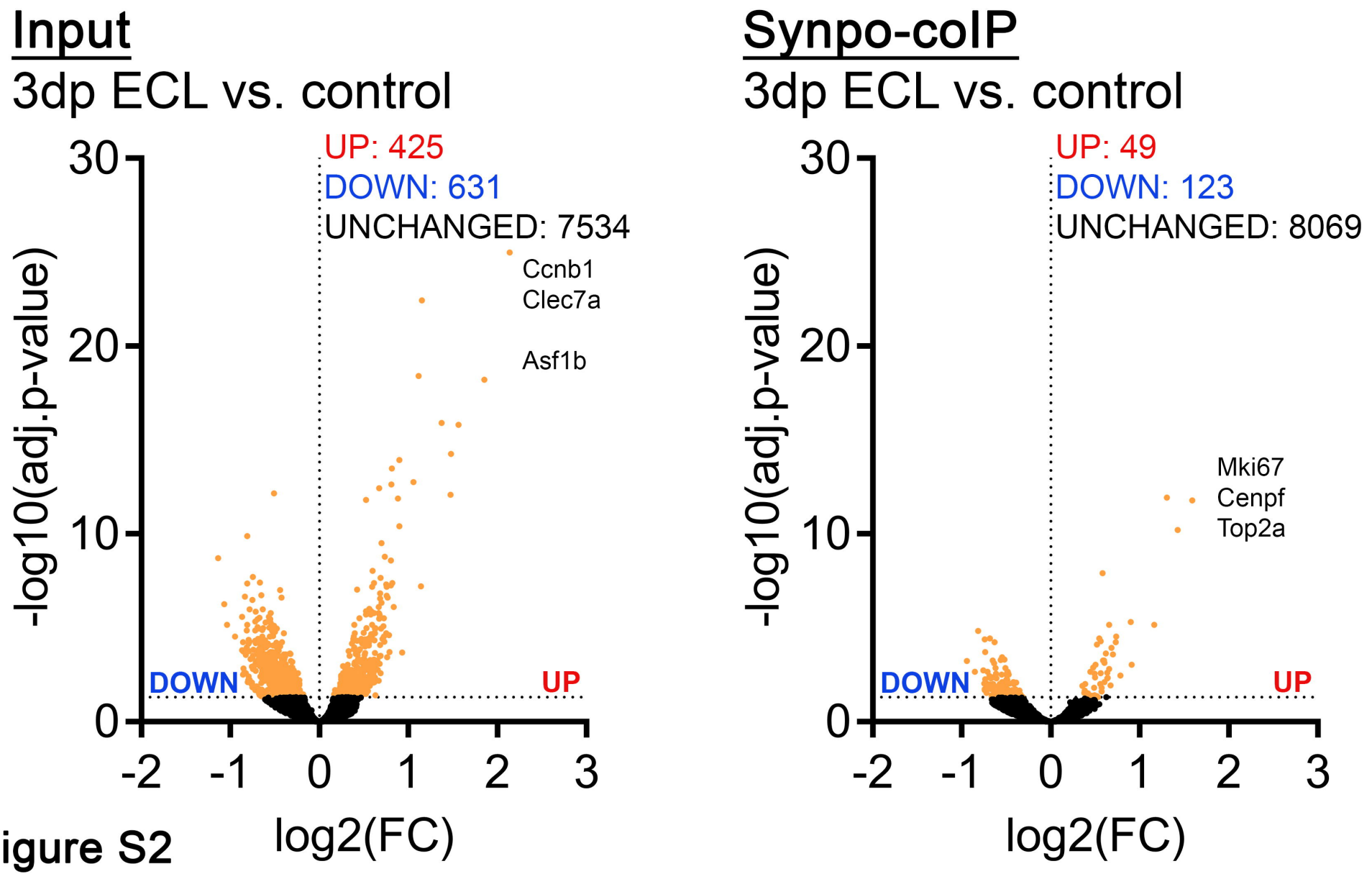
Input
3dp ECL vs. control
UP: 425
DOWN: 631
UNCHANGED: 7534
Ccnb1
Clec7a
Asf1b
DOWN
UP
-log10(adj.p-value)
log2(FC)
Synpo-coIP
3dp ECL vs. control
UP: 49
DOWN: 123
UNCHANGED: 8069
Mki67
Cenpf
Top2a
DOWN
UP
-log10(adj.p-value)
log2(FC)

Figure S2

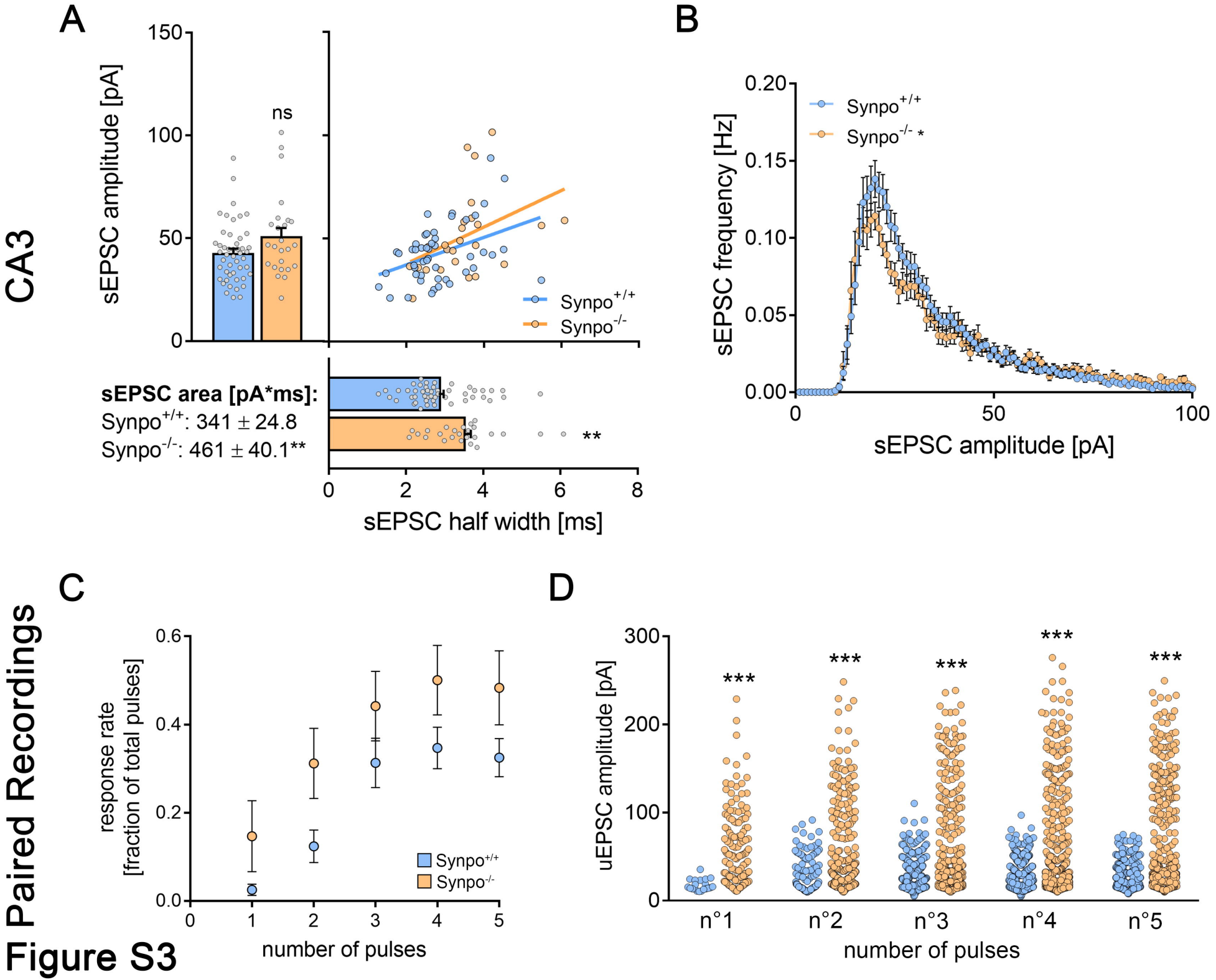
A
CA3
sEPSC amplitude [pA]
150
100
50
0
ns
Synpo+/+
Synpo-/-
sEPSC area [pA*ms]:
Synpo+/+: 341 ± 24.8
Synpo-/-: 461 ± 40.1**
**
0
2
4
6
8
sEPSC half width [ms]
B
sEPSC frequency [Hz]
0.20
0.15
0.10
0.05
0.00
Synpo+/+
Synpo-/- *
0
50
100
sEPSC amplitude [pA]
C
Paired Recordings
response rate
[fraction of total pulses]
0.6
0.4
0.2
0.0
Synpo+/+
Synpo-/-
0
1
2
3
4
5
number of pulses
D
uEPSC amplitude [pA]
300
200
100
0
***
n°1
n°2
n°3
n°4
n°5
number of pulses

Figure S3